Semiclassical study on tunneling processes via complex-domain chaos

T. Onishi,[1,*] A. Shudo,[1] K. S. Ikeda,[2] and K. Takahashi[3]
[1]*Department of Physics, Tokyo Metropolitan University, Minami-Ohsawa, Hachioji 192-0397, Japan*
[2]*Faculty of Science and Engineering, Ritsumeikan University, Noji-cho 1916, Kusatsu 525-0055, Japan*
[3]*The Physics Laboratories, Kyushu Institute of Technology, Kawazu 680-4, Iizuka 820-8502, Japan*
(Received 15 December 2002; revised manuscript received 20 May 2003; published 24 November 2003)

We investigate the semiclassical mechanism of tunneling processes in nonintegrable systems. The significant role of complex-phase-space chaos in the description of the tunneling processes is elucidated by studying a kicked scattering model. Behaviors of tunneling orbits are encoded into symbolic sequences based on the structure of a complex homoclinic tangle. By means of the symbolic coding, the phase space itineraries of tunneling orbits are related with the amounts of imaginary parts of actions gained by the orbits, so that the systematic search of dominant tunneling orbits becomes possible.

DOI: 10.1103/PhysRevE.68.056211 PACS number(s): 05.45.Mt, 03.65.Ge, 03.65.Sq, 05.10.−a

I. INTRODUCTION

Tunneling is one of the most typical and important phenomena in quantum physics, and for the past several years there is growing interest in natures of tunneling processes inherent in multidimensions. Quantum properties in multidimensional systems have been investigated extensively in terms of classical dynamical concepts in the field of *quantum chaos* [1], where the role of chaos, which is a generic property in multidimensional classical systems, has been elucidated. It was found that quantum tunnelings are also strongly influenced by whether underlying classical dynamics is chaotic or not [2–8], though tunneling processes have no classical counterpart.

Tunneling occurs typically between classical invariant components separated in phase space, such as between regular tori or chaotic seas. On one hand, mechanism of tunneling between distinct tori separated by chaotic seas has been studied in the context of *chaos-assisted tunneling* [4], and its semiquantum analysis has been done, in which the diffusion process in the chaotic sea accompanied with tunneling paths from and into the tori around the boundaries of the sea is considered to dominate the tunneling transport [6]. Experiments have also been performed by measuring microwave spectra in the superconducting cavity [9] and measuring momentum distributions of cold atoms, which was theoretically proposed in Ref. [10], in an amplitude-modulated standing wave of light [11,12].

On the other hand, tunneling between two chaotic seas separated by an energy barrier was studied by symmetric double wells [7]. It was shown that the spectra of tunnel splittings are reproduced by the orbits which consist of instanton processes under the barrier and homoclinic explorations in each chaotic well.

Generic aspects of the link between tunneling processes and real-domain ones in nonintegrable systems were examined in oscillatory scattering systems [13]. They made an energy-domain analysis for a model with continuous flows, while in the present study we make a time-domain one for a scattering map. The semiclassical interpretation of complicated wave functions was given in terms of oscillations of the stable manifold and an inherent property in flow systems, the divergent behavior of movable singularities of classical solutions on a complex time plane.

In the near-integrable regime, the role of resonances has been elucidated in the tunneling transport between symmetric tori by means of classical and quantum perturbation theories [14].

In any case, if one wants to know the mechanism of tunneling in chaotic systems by relating it with underlying classical structures, the use of complex orbits is inevitable [15], since tunneling is a purely quantum-mechanical process and is not describable in terms of real classical dynamics. Full account of such a process should, therefore, be given by *complex classical dynamics*. An attempt to make a full complex semiclassical analysis using the complex classical dynamics has been performed to understand which kinds of complex trajectories describe characteristic features of tunneling in the presence of chaos, and how the complex classical dynamics actually enters into real physical processes [5,16,17].

In Ref. [5], it was found that the initial values of orbits which play a semiclassically primary role form chainlike structures on an initial-value plane. A phenomenology describing tunneling in the presence of chaos based on such structures has been developed.

In Ref. [16], the first evidence was reported which demonstrates a crucial role of *complex-phase-space chaos* in the description of tunneling processes by analyzing a kicked scattering model. A hierarchy was found in the configurations of chainlike structures on the initial-value plane, and was interpreted as the manifestation of the emergence of chaos in the complex domain.

Very recently, the chainlike structures were shown to be closely related to the *Julia set* in complex dynamical systems [18]. The Julia set is defined as the boundary between the orbits which diverge to infinity and those which are bound for an indefinite time. Chaos occurs only on the Julia set [19]. In Ref. [18], it was proved that a class of orbits which potentially contribute to semiclassical wave functions is identified as the Julia set. It was also shown that the transi-

*Electronic address: t_onishi@comp.metro-u.ac.jp

tivity of dynamics and high density of trajectories on the Julia set characterize chaotic tunneling.

However, there still remains a problem in complex semiclassical descriptions. Dominant tunneling orbits are always characterized by a property that the amounts of imaginary parts of classical actions gained by the orbits are minimal among the whole candidates. It is, however, difficult to find such dominant orbits out of the candidates, because an exponential increase of the number of candidates with time prevents us from evaluating the amount of imaginary part of action for every candidate.

To solve this problem, in this paper, we investigate the structure of complex phase space for a kicked scattering model, and relate the structure to the amounts of imaginary parts of actions gained by tunneling orbits. Our main idea is to relate the symbolic dynamics of a homoclinic tangle emerging in complex domain to the behavior of tunneling orbits. It enables us to estimate the imaginary parts of actions gained by the orbits from symbolic sequences.

The organization of the paper is as follows. In Sec. II, the symbolic description of tunneling orbits is developed. This description requires an effective symbolic dynamics constructed on a complex homoclinic tangle. In this section, we emphasize the importance of the application of symbolic dynamics to tunneling problems, and the details of how we construct the symbolic dynamics itself is deferred to Sec. III. So it should be noted that in Sec. II we use the results in Sec. III without any technical details.

More precisely, in Sec. II, tunneling processes are investigated by a time-domain approach of complex semiclassical method. We introduce a scattering map which would be the simplest possible map modeling an energy-barrier tunneling in more than one degree of freedom. Though real-domain chaos is absent in this model, it is shown that tunneling wave functions exhibit the features possessed by the tunneling ones in the presence of real-domain chaos, such as the existence of plateaus and cliffs in the tunneling amplitudes and erratic oscillations on the plateaus.

It is elucidated that such tunneling features originate from chaotic classical dynamics in the complex domain; in other words, the emergence of a homoclinic tangle in the complex domain. The symbolic description of the tangle is introduced and is applied to the symbolic encoding of the behaviors exhibited by semiclassical candidate orbits. The amounts of imaginary parts of actions gained by the orbits are evaluated in terms of symbolic sequences assigned to the initial points of the orbits. Dominant tunneling orbits are determined according to the evaluated actions.

In the final part of Sec. II, tunneling wave functions are reproduced in terms of such dominant orbits, and the characteristic features appearing in tunneling amplitudes are explained by the interference among such dominant orbits.

In Sec. III, the technical aspects which are skipped in Sec. II are described in full detail. We first investigate the construction of a partition of complex phase space, which encodes the homoclinic points into symbolic sequences. Then some numerical observations are presented which relates the symbolic sequences and the locations of homoclinic points in phase space. On the basis of the observations, we study the relation between the symbolic sequences and the imaginary parts of actions for the homoclinic orbits. A symbolic formula for the estimation of imaginary parts of actions is finally derived.

In Sec. IV, we first conclude our present study, and then discuss the role of complex-domain chaos played in semiclassical descriptions of tunneling processes in nonintegrable systems. In a wide range of the tunneling processes, the important role of the complex-domain chaos is suggested. Finally some future problems are presented.

II. SEMICLASSICAL STUDY ON TUNNELING PROCESSES VIA COMPLEX-DOMAIN CHAOS

A. Tunneling in a kicked scattering model

We introduce a model which will be used in our study. The Hamiltonian of the model is given as follows:

$$\mathcal{H}(q,p,t)=T(p)+V(q)\sum_{n=-\infty}^{+\infty}\delta(t-n), \tag{1a}$$

$$T(p)=p^2/2, \tag{1b}$$

$$V(q)=k\exp(-\gamma q^2), \tag{1c}$$

where k and γ are some parameters with positive values, and the height and width of an energy barrier are given by k and $1/\sqrt{2\gamma}$, respectively. A set of classical equations of motion is given by

$$(q_{j+1},p_{j+1})=f(q_j,p_j), \tag{2a}$$

$$f:\mathbb{R}^2\to\mathbb{R}^2|(q,p)\mapsto(q+T'(p),p-V'(q+p)), \tag{2b}$$

where j is an integer denoting a time step and the prime denotes a differentiation with respect to the corresponding argument. $\mathbb{R}^2$ denotes real phase space.

This model has the following characteristics. First, no chaotic motion and no periodic orbit except a fixed point $(q,p)=(0,0)$ is found in real phase space, in contrast to, e.g., the real phase space of the standard map [20]. Such a simple situation can always be realized when $V(q)$ is unimodal (see Appendix A). Of course, topological entropy in real phase space is null. Second, no singularity is found in the solutions of Eq. (2) when f is extended to $\mathbb{C}^2$, since our $V(q)$ is an entire function. As seen later, the structure of complex phase space is our main concern. However, the singularities would make the structure overcomplicated. The present study focuses on the features of wave functions which are observed irrespective of the existence of singularities in $V(q)$, e.g., observed for our $V(q)$ and $V(q)=k\,\mathrm{sech}^2\gamma q$ which has singularities at $q=i\pi(n+1/2)/\gamma$ $(k,\gamma>0,n\in\mathbb{Z})$. Hence our model is suitable to study typical aspects of energy-barrier-tunneling processes without real-domain chaos. For our analysis to be generic, consideration must be given to the case of real-domain chaos. In the aspect of the number of semiclassically significant orbits, differences do exist between such case and our case, as mentioned in Sec. II F.

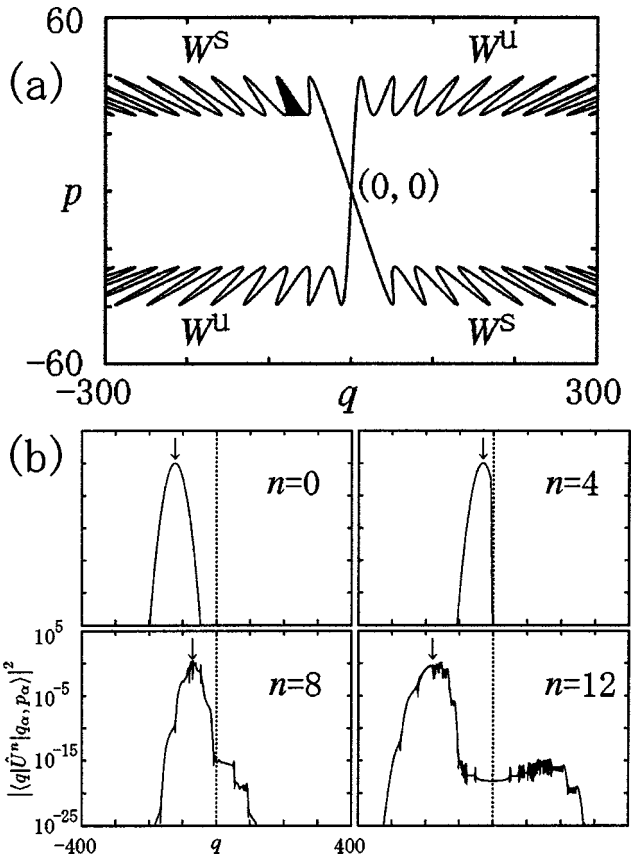

FIG. 1. (a) Real-domain stable and unstable manifolds of the origin ($k=500$, $\gamma=0.005$). The origin is an unstable fixed point when $k,\gamma>0$. (b) The time dependence of the wave function, evaluated quantum mechanically for $n=0$–12 in every four time steps [$\hbar=1$, $\sigma=10$, $q_\alpha=-123$, $p_\alpha=23$, with the same k and γ as in (a)]. Dotted lines represent $q=0$. The center of mass, whose positions are indicated by arrows, is reflected by the potential barrier, and so the amplitudes observed in the transmitted region represent tunneling effects. A characteristic action of the classical system, which we evaluated numerically by the phase-space area corresponding to a single oscillation of the stable manifold [the hatched area in (a)], is 153.

However, the study in our case is necessary for the first step to the semiclassical understanding of energy-barrier tunneling in nonintegrable systems.

Figure 1(a) shows the real phase space of our model. The stable and unstable manifolds of the fixed point at the origin are denoted by $\mathcal{W}^s$ and $\mathcal{W}^u$, respectively. As a direct consequence of the absence of real-domain chaos, both manifolds do not create homoclinic intersections.

The quantum-mechanical propagation for a single time step is given by the unitary operator

$$\hat{U}=\exp\left[-\frac{i}{\hbar}V(\hat{q})\right]\exp\left[-\frac{i}{\hbar}T(\hat{p})\right], \tag{3}$$

where $\hat{q}$ and $\hat{p}$ denote position and momentum operators, respectively, which satisfy the uncertainty relation $[\hat{q},\hat{p}]=i\hbar$. An incident wave packet is given by a coherent state of the form

$$\langle q|q_\alpha,p_\alpha\rangle=\frac{1}{(\pi\hbar\sigma^2)^{1/4}}\exp\left[-\frac{(q-q_\alpha)^2}{2\hbar\sigma^2}-i\frac{p_\alpha(q_\alpha-2q)}{2\hbar}\right], \tag{4}$$

where σ is a positive parameter and the width of the wave packet in the q direction is given by $\sqrt{\hbar}\sigma$. q_α and p_α are the position and momentum of the center of mass, respectively. Figure 1(b) shows the propagation of the wave packet [see also Fig. 6(a) for an enlarged one].

Our semiclassical argument based on the analysis formulated in Sec. II B requires a large amount of numerical trial and errors even for a single set of parameter values. Throughout the present study, we fixed the parameters $k,\gamma,\sigma,q_\alpha,p_\alpha$, and $\hbar$, as given in Fig. 1. The parameter values selected here are favorable to us in the following senses. First, $\hbar=1$ realizes large tunneling amplitudes, though the system is in the semiclassical regime. In fact, it is observed that the minimum tunneling actions [$\sim 10^1$; see the caption of Fig. 6(b)] are much smaller than the characteristic action of real-domain classical dynamics ($\sim 10^2$), as given in the caption of Fig. 1(b). The instanton trajectory of an integrable limit with null energy has the imaginary part of action, $\mathrm{Im}\int_{-\infty}^{+\infty}[T(p)-V(q)]p^{-1}dq=\sqrt{4\pi k/\gamma}\approx 1121$, however, this action is not useful for estimating the minimum tunneling actions in our time-domain approach. Second, large k makes complex classical dynamics highly unstable and then allows us to discuss the symbolic coding of complex orbits. The other parameters were selected to fit simultaneously the configuration of scattering problems and our requirements that tunneling processes occur as early as possible in order to reduce the amount of semiclassical computations.

Tunneling wave functions in Fig. 1(b) exhibit amplitude crossovers, plateaus and cliffs, and erratic oscillations on the plateaus. The same features have been reported in the case of dynamical tunneling processes in mixed phase space [5]. These are called the ''plateau-cliff structure,'' which has been confirmed in several systems as a typical structure of tunneling wave functions in the presence of real-domain chaos [5]. However, as seen in our model, the existence of the plateau-cliff structure does not always need chaotic dynamics in real phase space. So, the features of wave functions observed here would be beyond our intuitive expectation based on the real classical dynamics. This strongly motivates the use of complex trajectories and complex semiclassical analysis.

B. Formulation of complex semiclassical analysis

To simplify our formulation, we begin with the definition of a pair of canonical variables

$$(Q,P)=\frac{\sigma}{\sqrt{2}}(-ip+q\sigma^{-2},p-iq\sigma^{-2}). \tag{5}$$

For (q_0,p_0) and (q_α,p_α), which are the initial values of the map f and the center of wave packet (4), respectively, we denote

$$(Q_0,P_0)=(Q(q_0,p_0),\ P(q_0,p_0)), \tag{6a}$$

$$(Q_\alpha, P_\alpha) = (Q(q_\alpha, p_\alpha), P(q_\alpha, p_\alpha)). \tag{6b}$$

The wave function $\langle q|U^n|q_\alpha, p_\alpha\rangle$ is represented by the n-fold multiple integral

$$A_n \int dq_0 \cdots dq_{n-1} \exp\frac{i}{\hbar} S_n, \tag{7}$$

which is a discrete analog of Feynman path integral, where

$$A_n = (\pi\hbar\sigma^2)^{-1/4}(2\pi i\hbar)^{-n/2}, \tag{8a}$$

$$S_n = \sum_{j=0}^{n} L_j, \tag{8b}$$

$$L_j = T(p_{j-1}) - V(q_j) (j \geqslant 1, p_{j-1} = q_j - q_{j-1}), \tag{8c}$$

$$L_0 = i(q_0 - c_+ P_\alpha)(q_0 - c_- P_\alpha)/(2\sigma^2) - Q_\alpha P_\alpha/2$$

$$[c_\pm = i\sigma(\sqrt{2} \pm 1)]. \tag{8d}$$

The saddle point approximation for the integral is implemented to derive the semiclassical Van Vleck's formula, in which the wave function is expressed by purely classical-dynamical quantities. Each saddle point $(q_0, \ldots, q_{n-1}) \in \mathbb{C}^n$ should satisfy a set of classical equations of motion and boundary conditions

$$(q_{j+1}, p_{j+1}) = f(q_j, p_j) \quad (0 \leqslant j < n), \tag{9a}$$

$$(q_0, p_0) \quad \in \mathcal{I}, \tag{9b}$$

$$(q_n, p_n) \in \mathcal{F}, \tag{9c}$$

where $f: \mathbb{C}^2 \to \mathbb{C}^2$ is the classical map extended into complex phase space, and $\mathcal{I}$, $\mathcal{F}$ stand for manifolds defined by

$$\mathcal{I} = \{(q,p) \in \mathbb{C}^2 | P(q,p) = P_\alpha\}, \tag{10a}$$

$$\mathcal{F} = \{(q,p) \in \mathbb{C}^2 | \mathrm{Im}\, q = 0\}. \tag{10b}$$

Since the initial "momentum" P_0 is fixed by Eq. (10a), the shooting problem (9) will be solved by adjusting the initial "position" Q_0 in $\mathcal{I}$. Condition (9c) is required since we want to see here the wave function as a function of a real final position q_n. A set of initial points satisfying Eqs. (9) is given by

$$\mathcal{M}_n = \mathcal{I} \cap f^{-n}(\mathcal{F}). \tag{11}$$

Then the semiclassical Van Vleck's formula of $\langle q_n|U^n|q_\alpha, p_\alpha\rangle$ takes the form

$$(2\pi\hbar)^{-1/4} \sum_{(q_0,p_0) \in \mathcal{M}_n} \left| \frac{\partial^2 G_n}{\partial q_n \partial P_\alpha} \right|^{1/2} \exp\frac{i}{\hbar}\left(S_n - \frac{\phi_n}{2} \right), \tag{12}$$

where the sum is over the complex orbits whose initial points are located on $\mathcal{M}_n$ just defined. $\phi_n(q_0, p_0)$ is the Maslov index of each complex orbit. $G_n(q_n, P_0) = S_n + i(q_0 - c_+ P_0)(q_0 - c_- P_0)/(2\sigma^2)$ is a generating function which yields a set of canonical transformations $\partial G_n/\partial q_n|_{P_0} = p_n$ and $\partial G_n/\partial P_0|_{q_n} = -Q_0$. The outline of the derivation of Eq. (12) follows the conventional one [21], so we omit the description of it. For details, readers refer to the Appendix of Ref. [5].

C. Hierarchical configuration of initial values

The complex phase space of model (1) has a complicated structure in contrast to the real phase space. Figure 2(a) shows a typical pattern of $\mathcal{M}_n$, which consists of a huge number of strings. The finest scale structure of $\mathcal{M}_n$ is shown schematically in Fig. 2(b). Each string covers the whole range $(-\infty, +\infty)$ of the final q_n axis, so we call it a *branch*. In the latter figure, branches are linked to each other in the horizontal direction with narrow gaps, and they are said to form a *chainlike structure* [5,16] (the authors in Ref. [5] called it a *Laputa chain*). Our classical and semiclassical discussions are concerned with the branches which form chainlike structures. The other branches are found in both sides of each chainlike structure, which look like a pair of sea anemones as shown in the left-hand inset of Fig. 2(a) [they are omitted in Figs. 2(b) and 2(d)]. The semiclassical contribution from them is negligible, see the discussion in Sec. II F. Here we will explain the morphology of $\mathcal{M}_n$ in terms of these notions, and by relating it to the manifolds $\mathcal{W}^s$ and $\mathcal{W}^u$ which are extended to the complex domain. More precisely, the following three facts will be explained: First, the chainlike structure is created by the orbits propagating along $\mathcal{W}^s$ and $\mathcal{W}^u$; second, branches in $\mathcal{M}_n$ have a hierarchical configuration on $\mathcal{I}$; and third, the intersection

$$M = \mathcal{I} \cap \mathcal{W}^s, \tag{13}$$

is the main frame of the configuration of branches. Hereafter we identify $\mathbb{C}^2$ with $\mathbb{R}^4$, and mean a "curve" as a one-dimensional manifold in $\mathbb{R}^4$, and a "disk" as a two-dimensional one in there.

When the map f in Eqs. (2) is extended to $\mathbb{C}^2$, both $\mathcal{W}^s$ and $\mathcal{W}^u$ are two-dimensional manifolds in there at least locally. Since $\mathcal{I}$ is also a two-dimensional manifold, the dimension of the intersection M is lower than 1 in general, i.e., the intersection is neither a set of curves nor a surface, but may be fractal such as the Cantor set, the Hausdorf dimension of which is less than one.

We begin with the creation of the chainlike structure. For a point in $\mathcal{W}^s$ denoted by w and a small disk Δ which includes w, the dynamics of Δ is described as follows. By definition, the orbit of w converges to the origin. Also $f^k(\Delta)$ first approaches the origin as k increases, however, it in turn spreads along $\mathcal{W}^u$, and finally almost converges to $\mathcal{W}^u$.

This process is described in more detail. For $k \gg 1$, the intersection between $f^k(\Delta)$ and the neighborhood of $f^k(w)$ is approximated by a small disk Δ' which is tangent to $\mathcal{W}^u$ at the origin. Then the points on Δ' are parametrized by a small complex number z such that $(q(z), p(z)) = (z, (\lambda - 1)z)$, where λ is the maximal eigenvalue of the tangent map of f at the origin and is a real number. The q component of $f^m(q(z), p(z))$, denoted by $q_m(z)$, is a holomorphic function

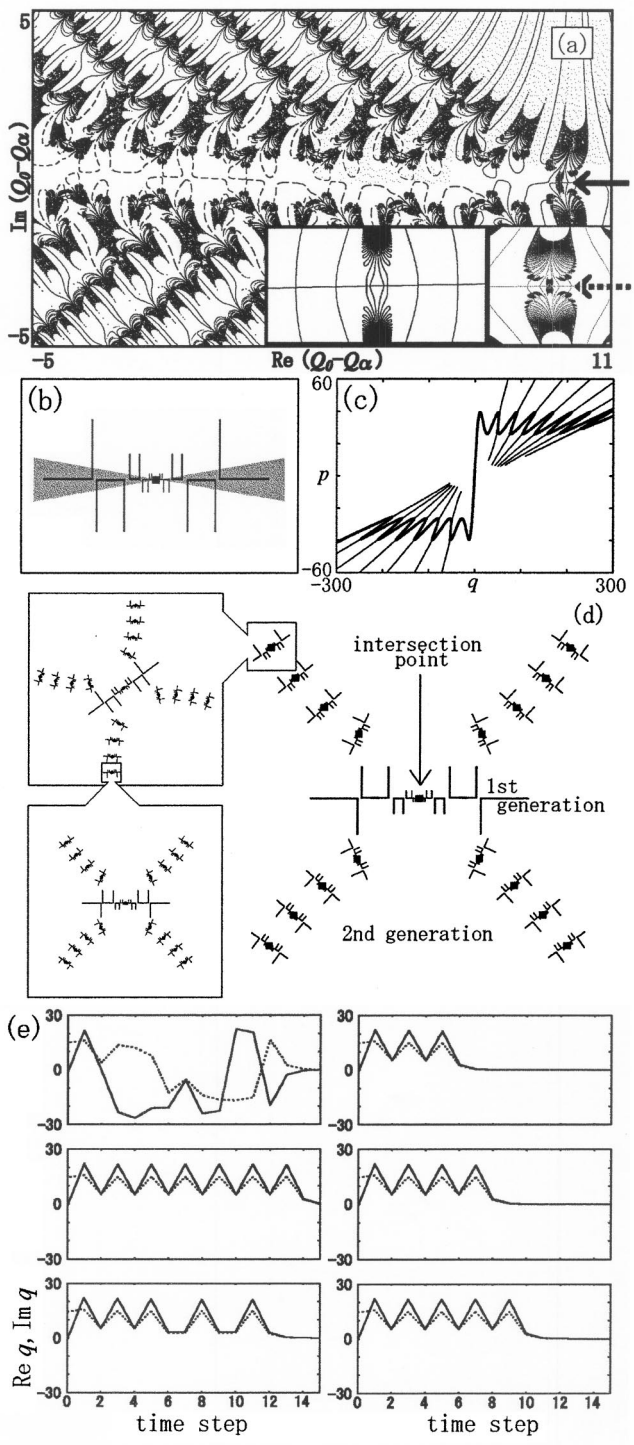

FIG. 2. (a) $\mathcal{M}_n$ for $n=10$ plotted on $\mathcal{I}$. Broken curves around $\mathrm{Im}(Q_0-Q_\alpha)=0$ are the branches finally used for the construction of semiclassical wave functions (see Fig. 6). There are two insets: the right-hand one enlarging a small area indicated by a solid arrow and the left-hand one enlarging a small area indicated by a dotted arrow. (b) Schematic representation of branches which form the horizontal center line in the left-hand inset of (a). The center dot represents an element of M defined in Eq. (13). Hatched and nonhatched parts are mapped by f^n to the bold and thin parts in (c), respectively. There is a caustic Q_0 defined by $\partial q_n/\partial Q_0|_{P_0}=0$ in a narrow gap between every neighboring branches. (c) The images of the branches in (b) by f^n for $n=10$, projected on real phase space. Bold and thin parts almost agree with the real domain $\mathcal{W}^u$ and the nonreal $\mathcal{W}^u$, respectively (for the real domain $\mathcal{W}^u$, see Fig. 1). The parts of images which have quite large $|\mathrm{Im}p_n|$'s are omitted. The creation of caustics in (b) are due to the oscillations of the real-domain $\mathcal{W}^u$. (d) The configuration of chainlike structures included in the right-hand inset of (a). A solid square at the center of each chainlike structure represents an element of M. (e) A variety of behaviors exhibited by orbits launching from M. Solid and broken lines represent $\mathrm{Re}\,q$ and $\mathrm{Im}\,q$, respectively. In the right column, the initial points of the trajectories belong to the sixth, eighth, and tenth generations, respectively, from top to bottom.

of z for any $m>0$. Then due to the reflection principle of holomorphic functions, the intersection $\Delta' \cap f^{-m}(\mathcal{F})$ [see Eq. (10) for the definition of $\mathcal{F}$] includes, on the z plane, the real axis $\mathrm{Im}\,z=0$, and a set of curves symmetric about the axis and perpendicular to the axis at the points satisfying $dq_m(z)/dz=0$.

The approximation used above allows one to consider that $\Delta \cap f^{-n}(\mathcal{F})$ for $n=k+m$ includes $f^{-k}(\Delta' \cap f^{-m}(\mathcal{F}))$. Replacing f^k around w by its linear approximation, and taking Q_0 as a coordinate on Δ, one can relate Q_0 and z linearly. Then in a similar way, $\Delta \cap f^{-n}(\mathcal{F})$ includes, on the Q_0 plane, a line through w and a set of curves symmetric about the line and perpendicular to the line at the points satisfying $dq_n(Q_0)/dQ_0=0$. The last equation is equivalent to the condition which defines caustics on $\mathcal{I}$ in the original problem (9). Finally, by taking Δ on $\mathcal{I}$, the configuration of a line and curves on the Q_0 plane just described explains the creation of a chainlike structure.

The mechanism mentioned above suggests that chainlike structures are created around any elements of M as the time

step increases. We numerically confirmed that the inverse is true, that is, any chainlike structures are created around elements of M, as shown in Fig. 2(b). Figure 2(c) shows that $f^n(\Delta)$ almost converges $\mathcal{W}^u$ even for $n=10$. In this way, the creation of chainlike structures is explained by the dynamics of a small disk first approaching real phase space with the guide of $\mathcal{W}^s$, then spreading over $\mathcal{W}^u$. It should be noted that this process is not specific to our dynamics, but is the one that the stable and unstable manifolds always have. Hence the process can take place also in real-domain dynamics and even in integrable one, whether one takes time-domain approaches or energy-domain ones [13].

Next we discuss the configuration of branches on $\mathcal{I}$. Figure 2(d) shows the schematic representation of chainlike structures in $\mathcal{M}_n$. As shown there, small chainlike structures are arranged on both sides of the central large one, and the same arrangement repeats around each of the small chainlike structures. This observation means that the branches in $\mathcal{M}_n$ have a hierarchical configuration. Then it may be natural to assign a *generation* to each chainlike structure in the hierarchy. For example, in Fig. 2(d), we can say that the first four generations are displayed.

Since chainlike structures are created around elements of M, these elements also have a hierarchical configuration as shown in Fig. 2(d), and it can be said that M constitutes the main frame of $\mathcal{M}_n$. Generations are assigned to the elements of M in the same way as to chainlike structures. The structure of the orbits launched from M is important for our semiclassical analysis because of the following reasons. The first is that these orbits describe well the behaviors of the orbits launched from chainlike structures toward real phase space. The second is that the study of orbits on the stable (or unstable) manifold is suitable for more canonical arguments since they are compatible with the theory of dynamical systems [22].

Figure 2(e) shows a variety of itineraries of the orbits launched from M. In the left column, the top row shows a typical behavior observed in M, where both $\mathrm{Re}\, q$ and $\mathrm{Im}\, q$ oscillate in an erratic manner for some initial time steps and eventually approach the origin. Regular itineraries such as periodic oscillations coexist among stochastic itineraries as shown in the middle row, where an approximately two-periodic behavior is seen. Another type of orbit is shown in the bottom row, where the trajectory first oscillates with period 2 and then turns into a three-periodic motion. The close relation between itinerating behaviors and the notion of generation can be seen clearly in the case of periodic oscillations, as shown in the right column of the figure. In each row, the length of time for which a trajectory keeps oscillating agrees with the generation of the initial point of the trajectory.

D. Emergence of a homoclinic tangle in complex phase space

The hierarchical structure of M is the manifestation of chaos. To see this, two facts are shown here. The first is that the homoclinic tangle of $\mathcal{W}^s$ and $\mathcal{W}^u$ emerges in complex phase space. The second is that the hierarchical structure of M is created as a consequence of the emergence of the tangle.

We study phase-space structures in terms of a coordinate on $\mathcal{W}^s$ defined as follows. Let Φ be a conjugation map from $\mathbb{C}$ to $\mathcal{W}^s$, which satisfies the relation

$$(\Phi^{-1} f \Phi)(\xi) = \lambda^{-1}\xi \quad \text{for} \quad \xi \in \mathbb{C}, \tag{14}$$

where λ denotes the maximal eigenvalue of the tangent map of f at the origin [23]. The ξ coordinate is normalized in the sense that f is represented by a linear transformation on the coordinate. Note that a similar coordinate is defined on $\mathcal{W}^u$ by taking $\Phi: \mathbb{C} \to \mathcal{W}^u$ and replacing λ^{-1} in Eq. (14) by λ. Hereafter we denote $\lambda^{-1}\xi = f_s(\xi)$.

Figure 3(a) shows a set of homoclinic points of the origin, obtained numerically on the ξ coordinate. In the figure, enlarging the neighborhood of any homoclinic point, one can find the configuration of homoclinic points similar to the original one with finer scale [for enlarged figures, see Fig. 4(b)]. The set of homoclinic points looks basically the same on $\mathcal{W}^u$, and also one can find there the self-similarity just described. Hence it is numerically confirmed that a *homoclinic tangle* emerges in complex phase space. The present model tells us that null topological entropy in real phase space does not always exclude the existence of chaos in complex domain.

Figure 3(b) shows M plotted on the same coordinate with different scale. Similarity to Fig. 3(a) is evident, which suggests that the creation of the hierarchical configuration of M, as shown in Fig. 2(d), is due to the emergence of the homoclinic tangle in complex domain. The relation between the structures of M and of the homoclinic tangle is made more clear by the notion of generation introduced in Sec. II C. To see the relation, we give the precise definition of generations. Let D be a connected domain in the ξ plane which satisfies the conditions

$$(0,0) \in D, \tag{15a}$$

$$f_s(D) \subset D. \tag{15b}$$

Denoting $D' = D - f_s(D)$, the ξ plane is decomposed into a family of disjoint domains as follows:

$$\bigsqcup_{n \in \mathbf{Z}} f_s^n(D') = \mathbb{C} - \{(0,0)\}, \tag{16a}$$

$$f_s^m(D') \cap f_s^n(D') = \phi \quad (m \neq n). \tag{16b}$$

Thus for any point ξ in this plane except $(0,0)$, there exists a unique integer n such that $\xi \in f_s^{-n}(D')$. Then the generation of the point ξ is defined as the integer n. This definition allows us to assign generations to the homoclinic points.

Figure 3(a) shows the shape of D. Note that under the conditions in Eqs. (15), the relations in Eqs. (16) hold irrespective of the shape. In our earlier publication [16], D was chosen as a disk. In the present study, another choice of D is proposed. We describe the shape in a specified manner in Sec. II.

For any point in D which is sufficiently close to $\xi = (0,0)$, the forward orbit approaches the origin straightforwardly at an exponential rate in the original coordinate

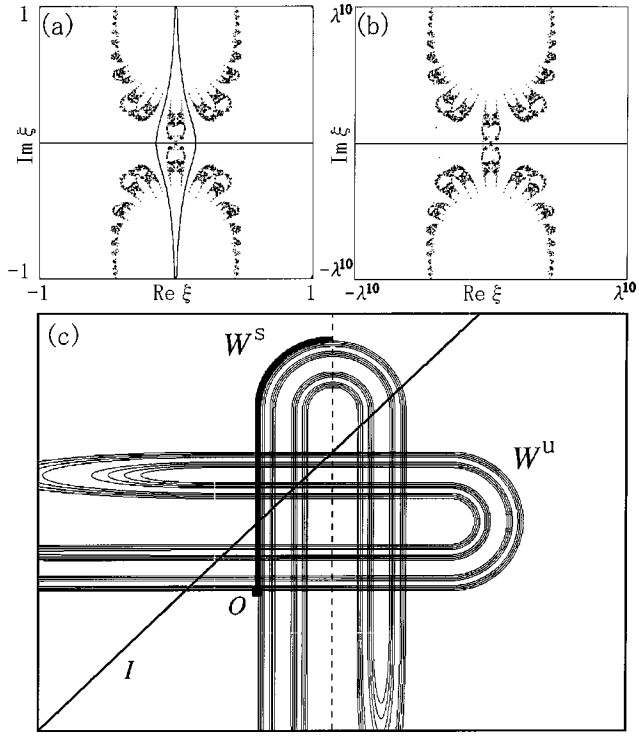

FIG. 3. (a) The set of homoclinic points, $\mathcal{W}^s \cap \mathcal{W}^u$, plotted on $\mathcal{W}^s$. The center of the figure corresponds to $(q,p)=(0,0)$, and the points on the horizontal axis are included in real phase space. The domain D in Eq. (15) is enclosed by solid curves. (b) The intersection M plotted on $\mathcal{W}^s$. (c) The horse-shoe map on a plane. $\mathcal{W}^s$ and $\mathcal{W}^u$ for a fixed point O creates a homoclinic tangle. A solid line across the tangle and a bold curve on $\mathcal{W}^s$ are analogous with our $\mathcal{I}$ and D, respectively. A dotted line is the boundary of partition which creates binary codes. Due to the horse-shoe dynamics, $\mathcal{W}^s$ in the nth generation has 2^n intersection points with $\mathcal{I}$.

(q,p). For any point in the nth generation $(n \geqslant 1)$, it takes at least n steps until the orbit starts to approach the origin exponentially, and thus it can exhibit a variety of behaviors during its itinerary. That is why the oscillations shown in Fig. 2(e) are related with the generations.

The similarity between Figs. 3(a) and 3(b) suggests that the behaviors of orbits launched from M are similar to those of homoclinic orbits. Actually, we numerically checked that for any element of M, a homoclinic point is found in the same generation as the element, such that the orbit of the element is well approximated by the homoclinic orbit. This is the working principle of our symbolic description for the elements of M, as seen later. Therefore the hierarchical configuration of M displayed on $\mathcal{I}$ represents, via similarity between M and a set of homoclinic points, the structure of the homoclinic tangle, in other words, is a piece of evidence for complex-domain chaos.

More generically, one can say that the hierarchical configuration of M on $\mathcal{I}$ is the manifestation of chaos, whether the configuration emerges in real domain or in complex domain. Figure 3(c) shows an analogy of our present situation with a horse-shoe map on a plane. In the case of this map, $\mathcal{I} \cap \mathcal{W}^s$ and $\mathcal{I} \cap \mathcal{W}^u$ form the Cantor sets, and the fractal structures of these intersections are originated from the

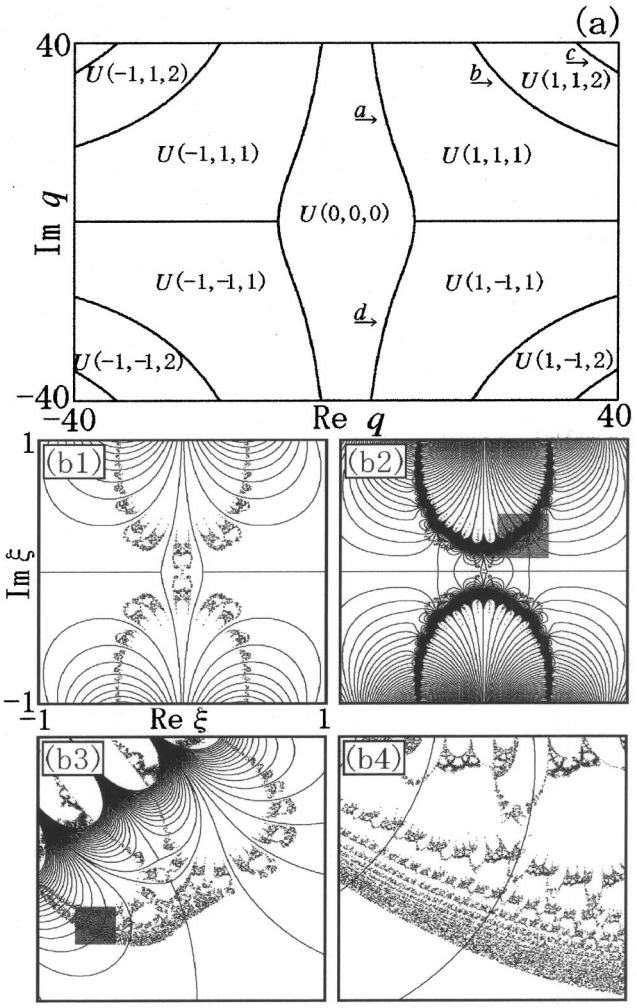

FIG. 4. (a) Intersection between the q plane and the boundaries of the partition. Each boundary is a three-dimensional manifold according to Eq. (19), so that the intersection is a set of curves. The curves labeled by a,b,c, and d indicate the boundaries with $(x,y,\nu)=(1,1,1),(1,1,2),(1,1,3)$, and $(1,-1,1)$, respectively. (b) Boundaries of (b1) $\mathcal{P}$ and (b2) $f(\mathcal{P})$ plotted in the same range of the ξ plane, with homoclinic points superposed. The generations of the homoclinic points displayed are lower than or equal to 1. (b3) The enlarged figure of the hatched part of (b2). The boundaries of $f(\mathcal{P})$ fail to divide the set of homoclinic points clearly, in the hatched part of (b3). (b4) The enlarged figure of the hatched part of (b3). Homoclinic points are aggregated densely like a thick band. The boundary curves might touch the set of homoclinic points.

tangle of $\mathcal{W}^s$ and $\mathcal{W}^u$. Replacing $\mathbb{C}$ in Eq. (16a) by $\mathbb{R}$, one can define generations in a similar way.

Once we know that chaos exists also in the complex domain, the methodology studying chaos in the real domain can be applied to the analysis on the complex domain. In particular, symbolic dynamical description of orbits, which is available if one finds a proper partition of phase space to define it, is a standard technique in the theory of dynamical systems [22], and can be a very useful tool to analyze complicated phase-space structures. Homoclinic orbits are also describable in terms of the symbolic dynamics, so our strategy to study the hierarchical configuration of M hereafter is

to take the symbolic description of homoclinic orbits.

E. Symbolic description of complex orbits

We will explain the symbolic descriptions of complex homoclinic orbits and semiclassical candidate orbits. For the description of complex homoclinic orbits, we constructed symbolic dynamics which works effectively and estimated the imaginary parts of actions for the homoclinic orbits. The final results of this study are presented here, and the detailed explanation is given in Sec. III. On the basis of the results, the symbolic description of semiclassical candidate orbits is developed in the following way. First, the elements of M are encoded into symbolic sequences. We compare both configurations of homoclinic points and the elements of M, on the ξ coordinate defined on $\mathcal{W}^s$. A clear similarity between both configurations enables us to find, for each element of M, a homoclinic point located in the neighborhood of the element of M. Since the homoclinic point is already encoded into a symbolic sequence, we encode the element of M into this symbolic sequence. Next, semiclassical candidate orbits are encoded into symbolic sequences. Since the behaviors of orbits launched from a single chainlike structure are described by the orbit of an element of M located at the center of the chainlike structure, we assign the symbolic sequence of the element of M to all initial points in the chainlike structure.

Symbolic dynamics is usually constructed by finding a generating partition $\mathcal{G}$, which is the partition of phase space satisfying the relation

$$\bigvee_{n=-\infty}^{+\infty} f^n(\mathcal{G}) = \epsilon_0, \tag{17}$$

where the left-hand side (lhs) is the product of all partitions created by $f^n(\mathcal{G})$, and the right-hand side (rhs) is the partition of phase space into its individual points [22] (here we should consider the ''phase space'' as the closure of a set of homoclinic points of the origin). Roughly speaking, $\mathcal{G}$ is the partition of phase space such that each separated component of phase space corresponds to a symbol, and for every bi-infinite sequence of symbols there may at most exist one trajectory of the original map. In our case, a partition of complex phase space is defined in terms of the phase part of $V'(q)$ which appears in the form

$$V'(q) = -2\gamma k \exp[-A(q) - iB(q)], \tag{18}$$

where $A(q), B(q) \in \mathbb{R}$. The boundaries of the partition are defined by

$$\{(q,p) \in \mathbb{C}^2 | B(q) = [2\nu xy - (3x+1)y/2]\pi\}, \tag{19}$$

where (x,y,ν) is an element of the set

$$\mathcal{T} = \{(x,y,\nu) | (x,y) \in \{+1,-1\}, \nu \in \mathbb{N}\}. \tag{20}$$

The intersection between the q plane and the boundaries of the partition are shown in Fig. 4(a). x and y in Eq. (19) represent the signs of $\mathrm{Re}\, q$ and $\mathrm{Im}\, q$ of the points on a boundary respectively, i.e., the pair of x and y specifies the quadrant of the q plane where the q component of the boundary is included. ν is the squared ''distance'' between the boundary and the origin, in the sense that the axis $\mathrm{Re}\, q = \mathrm{Im}\, q$ on the q plane intersects the boundary at $q \approx (x\sqrt{\nu\pi/\gamma}, y\sqrt{\nu\pi/\gamma})$ for $\nu \gg 1$.

Then our partition, denoted by $\mathcal{P}$, is defined as a set of phase-space components as follows:

$$\mathcal{P} = \{U(x,y,\nu) | (x,y,\nu) \in \mathcal{S}\}, \tag{21a}$$

$$\mathcal{S} = \mathcal{T} \cup \{(0,0,0)\}, \tag{21b}$$

where $U(x,y,\nu)$ for $(x,y,\nu) \in \mathcal{T}$, whose q component is displayed in Fig. 4(a), denotes the region enclosed by two boundaries associated with (x,y,ν) and $(x,y,\nu+1)$, and $U(0,0,0)$ denotes the complement of the union of all phase-space components encoded to the elements of $\mathcal{T}$. The origin, $(q,p) = (0,0)$, is included in $U(0,0,0)$.

Figure 4(b) shows the ξ plane divided by $f^n(\mathcal{P})$ for $n = 0$ and 1. The central domain in Fig. 4(b1) is the domain D, which was introduced in Sec. II D. The domain D is defined on the ξ plane as a connected domain of $U(0,0,0) \cap \mathcal{W}^s$ which includes $\xi = 0$. If $f^n(\mathcal{P})$ for any $n \geqslant 0$ divides clearly the set of homoclinic points displayed here, then $\mathcal{P}$ is the generating partition, i.e., relation (17) holds for $\mathcal{P}$ [it is sufficient to consider the case of $n \geqslant 0$ since any homoclinic point is mapped to the region displayed in Fig. 4(b1) by the iterations of f].

On one hand, $f^n(\mathcal{P})$ for $n = 0$ divides a set of homoclinic points clearly as shown in Fig. 4(b1). This means that our partition is a reasonable approximation of the generating partition. So by means of $\mathcal{P}$, we can construct a symbolic dynamics which works effectively. On the other hand, there are some regions in the ξ plane where $f^n(\mathcal{P})$ for $n \geqslant 1$ fails to divide the set of homoclinic points clearly. In such regions, it may be necessary to improve our partition to obtain the generating partition, and it is our future problem. Note that our complex dynamics is not proved to be hyperbolic, and that the existence of the generating partition for nonhyperbolic systems is an open problem. The improvement of the partition is of mathematical interest, however, as actually demonstrated below, the present definition of $\mathcal{P}$ is sufficient for our semiclassical analysis.

In terms of $\mathcal{P}$, each homoclinic point is encoded into a bi-infinite symbolic sequence of the form

$$\ldots OOa_{-n}a_{-(n-1)} \ldots a_{-1}.a_0a_1 \ldots a_nOO \ldots, \tag{22}$$

where $O = (0,0,0)$, $n \in \mathbb{N}$, and $a_k \in \mathcal{S}(|k| \leqslant n)$. The symbol a_k represents that the image of the homoclinic point by f^k is included in a phase-space component $U(a_k)$ defined in Eqs. (21). The finite sequence of a_k's is accompanied with semi-infinite sequences of O's on both sides. It reflects that any homoclinic point approaches the origin of phase space by forward and backward iterations of f. In particular, homoclinic points included in D are encoded into symbolic sequences of the form

$$\ldots OOa_{-n}a_{-(n-1)} \ldots a_{-1}.OO \ldots, \tag{23}$$

where $n \in \mathbb{N}$ and $a_k \in \mathcal{S}(0<k\leqslant n)$. Any symbol on the rhs of the decimal point is O, since the forward orbits are always included in a component $U(O)$ due to Eq. (15b).

For a homoclinic point w, which has a symbolic sequence of form (22), let us consider the imaginary part of action of the form

$$s(w)=\sum_{k=1}^{+\infty} \mathrm{Im}[T(p_{k-1}(w))-V(q_k(w))], \qquad (24)$$

where $(q_k(w),p_k(w))$ stands for $f^k(w)$. When we denote $a_k=(x_k,y_k,\nu_k)$ for $k\in\mathbb{Z}$, $s(w)$ is estimated by

$$\frac{\pi}{\gamma}\sum_{k=1}^{+\infty}(x_k\nu_k^{1/2}-x_{k-1}\nu_{k-1}^{1/2})(y_k\nu_k^{1/2}-y_{k-1}\nu_{k-1}^{1/2}), \qquad (25)$$

where γ is a parameter of $V(q)$. The derivation of formula (25) is presented in Sec. III.

From these results, we discuss the symbolic description of semiclassical candidate orbits. Let M_n be a subset of M whose members belong to generations lower than n. Then we observe numerically the following two facts: first, the clear similarity between Figs. 3(a) and 3(b) enables us to find, for any element of M_n and in its neighborhood on the ξ plane, a homoclinic point which has a symbolic sequence of the form

$$\ldots OO.a_0a_1\ldots a_{n-3}OO\ldots \quad (a_{n-3}\neq O). \qquad (26)$$

For $n=2$, M_n has only a single element, and a homoclinic point which has $\ldots OO.O\ldots OO\ldots$ corresponds to the element. For $n=1$, M_n is a null set. Second, on the plane $\mathcal{I}$, the elements of M_n are located at the centers of chainlike structures in $\mathcal{M}_n$ [see Fig. 2(d)].

From the first fact, to each point of M_n, we assign a semi-infinite symbolic sequence of the form

$$a_0a_1\ldots a_{n-3}OO\ldots. \qquad (27)$$

Figure 5 shows some trajectories launched from M and symbolic sequences of form (27) assigned to the initial points of the trajectories. The signs and amplitudes of the q components at each time step are well described by (x,y)'s and ν's of the corresponding symbols. This means that the behaviors of forward orbits launched from M are well approximated by those of homoclinic orbits.

From the second fact, to each chainlike structure in $\mathcal{M}_n(\subset\mathcal{I})$, we assign the same symbolic sequence as the element of $M_n(\subset\mathcal{W}^s)$ located at the center of the chainlike structure. This assignment is reasonable since, as stated in Sec. II C, the motions of orbits launched from the chainlike structure are well approximated, till they start to spread over $\mathcal{W}^u$, by the motion of an orbit launched from the element of M. Then chainlike structures in $\mathcal{M}_n$ are also described by symbolic sequences of form (27).

For any trajectory launched from a single chainlike structure in $\mathcal{M}_n$, we approximate the imaginary part of action as that of the trajectory launching from the element of M_n located at the center of the chainlike structure. Hence, by using Eqs. (25)–(27), the estimation of the imaginary parts of actions for semiclassical candidate orbits is attributed to the estimation of those for homoclinic orbits. There are branches not included in any chainlike structure, and no symbolic sequence is assigned to them. However, semiclassical contributions from them are negligible. This issue is discussed in the following Sec. II F.

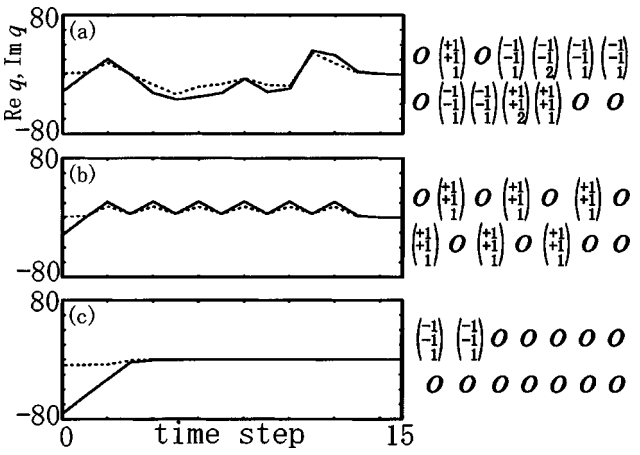

FIG. 5. The trajectories launched from M, and symbolic sequences assigned to their initial points (elements of each column vector are x,y, and ν from top to bottom). A semi-infinite part, $OOO\ldots$, is omitted in each sequence. Solid and broken lines represent $\mathrm{Re}\,q$ and $\mathrm{Im}\,q$, respectively. The trajectories show (a) erratic motions, (b) approximately two-periodic motions, and (c) monotonical approach to real phase space.

F. Reproduction of tunneling wave functions

Semiclassical wave functions are constructed from significant complex orbits selected according to the amounts of imaginary parts of actions. The semiclassical mechanism of the tunneling processes is explained by the structure of complex phase space.

The sum in Eq. (12) is evaluated in three steps: First, branches not included in chainlike structures are removed from $\mathcal{M}_n$; second, elements of $M_n(\subset M)$ are put in order according to the amounts of imaginary parts of actions estimated by Eq. (25); and finally, the sum is evaluated for the initial points in chainlike structures associated with the elements of M_n for which the above estimations are small.

The first step is necessary due to the following reason. For orbits launched from $\mathcal{M}_n$ but not from chainlike structures, there is no orbit launched from M which guides them to real phase space within n time steps. This means that these orbits have large imaginary parts of momenta at the time step n, so that they gain sufficiently large amounts of imaginary parts of actions. If the imaginary parts of actions are positively large, the contributions from the orbits are small enough to be negligible, or if they are negatively large the contributions from the orbits are unphysical due to the Stokes phenomenon [24], so that the orbits should be excluded from the whole candidates.

In the second step, some elements are removed from M_n also due to the Stokes phenomenon. Following the prescription given in Ref. [25], we found that chainlike structures

which have unphysical contributions to wave functions, including the case of exponentially large semiclassical amplitudes, are associated with the elements of M_n whose symbolic sequences include symbols of the form $(1,-1,\nu)$ or $(-1,1,\nu)$ with $\nu \in \mathbb{N}$. The justification is our future problem. See the Discussion in Sec. IV.

After removing such elements from M_n, we have the ordering for elements of M_n:

$$w_0 \; w_1 \; w_2 \ldots, \tag{28}$$

such that the inequalities hold:

$$0 \leqslant s(w_0) \leqslant s(w_1) \leqslant s(w_2) \leqslant \cdots, \tag{29}$$

where $s(w_k)$ for $k \geqslant 0$ represents the imaginary part of action estimated by Eq. (25) for the forward trajectory of w_k.

From Appendix B, it is seen that w_0, which is primarily significant in M_n for wave functions, has the symbolic sequence

$$OOO \ldots, \tag{30}$$

and the members of $\{w_1, w_2, \ldots, w_{2(n-2)}\}$, which are secondarily significant in M_n, have symbolic sequences of the form

$$bbb \ldots bbOOO \ldots, \tag{31}$$

where $b \in \{(1,1,1),(-1,-1,1)\}$, and the length of $bbb \ldots bb$ ranges from 1 to $n-2$. Due to form (27), the length is bounded above by $n-2$, and the member of $\{w_1, w_2, \ldots, w_{2(n-2)}\}$ which has $bbb \ldots bb$ of length $k-2 (k \leqslant n)$ belongs to the kth generation. Formula (25) tells us that $s(w_1) = s(w_2) = \cdots = s(w_{2(n-2)})$.

We observed that the orbits of $w_0, w_1, \ldots, w_{2(n-2)}$ behave as follows. The orbit of w_0 converges to the origin exponentially, so that it gains the smallest imaginary part of action. The orbits of $w_1, w_2, \ldots, w_{2(n-2)}$ first explore the vicinity of real phase space till the sequence $bbb \ldots bb$ terminates and then converge to the origin exponentially. Such motions yield much smaller imaginary parts of actions than flipping motions in complex domain, which are observed for generic trajectories launched from M. The motions of homoclinic orbits whose symbolic sequences include subsequences of form (31) are investigated in Sec. III. There it is found that such homoclinic orbits explore the vicinity of real phase space. The motions of the orbits of $w_1, w_2, \ldots, w_{2(n-2)}$ reflect those of homoclinic orbits.

Figure 6(a) shows quantum and semiclassical wave functions for $n=10$, the latter of which is constructed by taking account of the contributions from chainlike structures associated with $w_0, w_1, \ldots, w_{2(n-2)}$. Both functions are in excellent agreement. The contributions from the other chainlike structures are much smaller than those taken account of here. Their squared amplitudes are of the order of $\sim 10^{-50}$ at most. In particular, the contributions from trajectories which exhibit flipping or oscillatory motions are negligible, as shown in Fig. 6(c).

It is remarkable that only a small number of branches are significant to describe the tunneling processes [the significant branches are represented by broken curves in Fig. 2(a)]. More precisely, the numbers of branches that we need increases algebraically with time step n, while the total number of chainlike structures and that of branches in $\mathcal{M}_n$ increase exponentially with n. The algebraic increase of significant orbits results from linear increases of significant chainlike structures and of branches included in individual chainlike structures. The former linear increase is due to the symbolic form (31). The latter is due to the oscillating structure of real domain $\mathcal{W}^u$ by which the number of folding points of any manifold initially put in real domain increases at most linearly with time step. In other words, the algebraic increase is a consequence of the absence of real-domain chaos. When the real domain is chaotic, a small piece of a complex-domain manifold is, after it approached the real domain by the iterations of the map, stretched and folded by real-domain chaotic dynamics without gaining additional imaginary part of action, so that the number of significant orbits can increase exponentially with time [5,18]. It should be noted that in the integrable limit of our model, there is no increase in the number of branches with time. Hence in our case, the algebraic increase is the reflection of nonintegrability.

The excellent agreement between both quantum and semiclassical calculations enables us to interpret semiclassically the features of tunneling wave functions. Figure 6(b) clearly shows that the contributions from many chainlike structures reproduce the crossovers of amplitudes in reflected and transmitted regions. We found that erratic oscillations on each semiclassical component are due to the interferences between branches included in a single chainlike structure. Since the length of $bbb \ldots bb$ decides the generations of $w_1, w_2, \ldots, w_{2(n-2)}$, it can be said that the crossovers of amplitudes are created by the interferences between chainlike structures belonging to different generations. In this way, the complicated tunneling amplitudes are explained semiclassically by the creations of chainlike structures on the plane $\mathcal{I}$ and by the exponential increase of the number of chainlike structures with time (though linear increase for significant ones), which is due to the emergence of a complex homoclinic tangle.

The semiclassical mechanism of the tunneling processes in our model is summarized as follows. Stable and unstable manifolds of a real-domain unstable fixed point create a tangle in complex domain. The initial manifold representing a quantum initial state is located through the tangle, so that the intersection points between the initial manifold and the stable manifold form a hierarchical structure on the initial manifold. The orbits launched from the neighborhood of each intersection point are guided to real phase space by the stable manifold and then spread over the unstable manifold. The number of the orbits guided to real phase space increases exponentially with time (though significant ones increase algebraically), reflecting the hierarchical structure formed by the intersection points on the initial manifold. Then the interferences between these orbits create complicated patterns in the tunneling amplitudes.

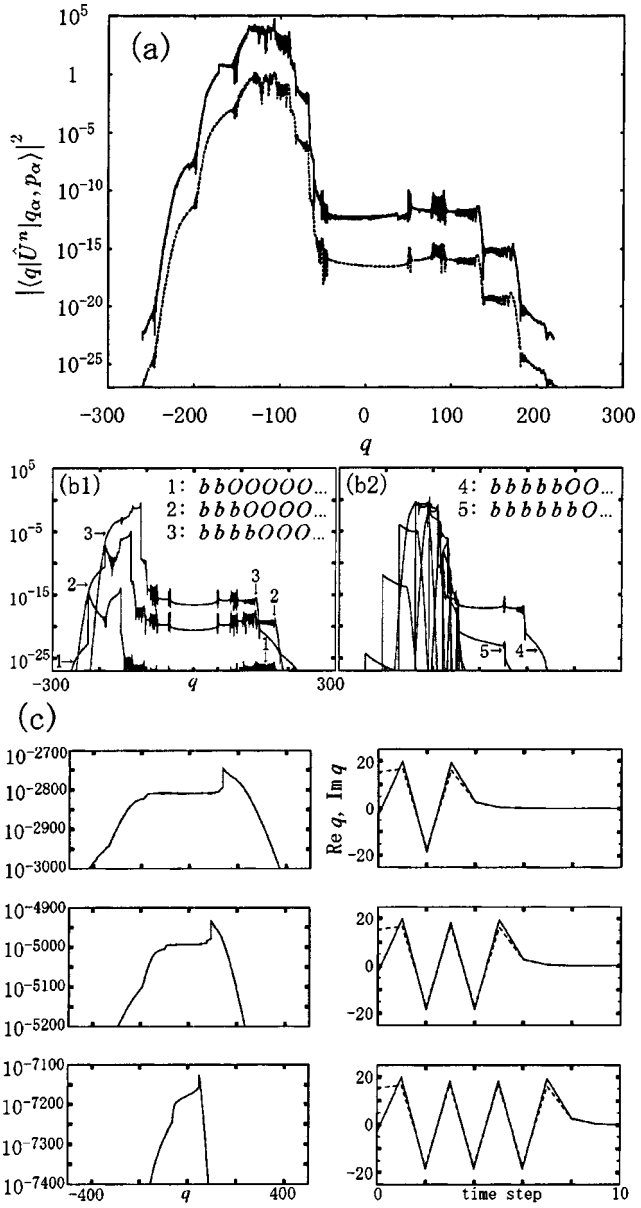

FIG. 6. (a) Quantum and semiclassical wave functions for $n=10$, represented by dotted and solid curves, respectively. The solid one is shifted by 10^4 to distinguish both functions. (b) Individual contributions from chainlike structures to the semiclassical wave function shown in (a). The crossovers of amplitudes far from the origin and near the origin are mainly reproduced by the components displayed in (b1) and (b2), respectively. For some components, symbolic sequences assigned to chainlike structures are presented, where $b=(-1,-1,1)$. Each of the components 1–5 is dominated by a single-orbit contribution at $q=0$, whose imaginary part of action is 26.9, 17.9, 14.3, 15.9, and 22.7, respectively. (c) Squared amplitudes of the semiclassical components (lhs) which come from chainlike structures associated with the elements of M whose trajectories exhibit oscillatory motions (rhs). Solid and broken lines on the rhs represent $\mathrm{Re}\,q$ and $\mathrm{Im}\,q$, respectively. Flipping or oscillatory motions in complex phase space gain large amounts of imaginary parts of actions due to large complex momenta.

III. SYMBOLIC DESCRIPTION OF A COMPLEX HOMOCLINIC TANGLE

A. Construction of partition of phase space

Here we construct a partition of complex phase space which encodes homoclinic points of the origin into symbolic sequences and defines symbolic dynamics which works effectively. The behaviors of homoclinic orbits and the evaluation of imaginary parts of actions for the orbits are presented in Secs. III B and III C, respectively.

There have been extensive studies on the construction of generating partition in real phase space [26] even in nonhyperbolic regimes [27]. In such real-domain studies, the boundaries of generating partition are roughly approximated by a set of folding points of flat manifolds, created by single-step iterations of maps. However, the extension of such working principle to complex phase space is not obvious.

In order to find the generating partition for our map f, we consider the single-step dynamics of f^{-1} for flat manifolds of the form $\{(q,p)\in\mathbb{C}^2|p=p_0\}$ with $p_0\in\mathbb{C}$. We found that the dynamics is well understood by relating it to the exponent $A(q)+iB(q)$ of $V'(q)$, where $A(q)=\gamma[(\mathrm{Re}\,q)^2-(\mathrm{Im}\,q)^2]-\ln|q|$ and $B(q)=2\gamma(\mathrm{Re}\,q)(\mathrm{Im}\,q)-\arg q$ [the notation is the same as in Eq. (18)]. The contour curves of both functions are shown in Figs. 7(a) and 7(b).

First, the single-step dynamics of f^{-1} is considered far from the origin, $(q,p)=(0,0)$, and then is considered around the origin. Far from the origin, $A(q)$ and $B(q)$ are controlled linearly by variables u and v:

$$(u,v)=([(\mathrm{Re}\,q)^2-(\mathrm{Im}\,q)^2]/2,(\mathrm{Re}\,q)(\mathrm{Im}\,q)). \quad (32)$$

On this coordinate, one obtains the estimations

$$A(q)=2\gamma u+O(\ln|u|)\ \ (v:\text{fixed},|u|\to\infty), \quad (33a)$$

$$B(q)=2\gamma v+O(\ln|v|)\ \ (u:\text{fixed},|v|\to\infty), \quad (33b)$$

$$\text{or}\quad 2\gamma v+O(|u|^{-1})\ \ (v:\text{fixed},|u|\to\infty), \quad (33c)$$

where γ is a parameter in $V(q)$.

In a region of phase space where $|u|\gg 1$, the dynamics of f^{-1} is discussed as follows. When $u\gg 1$, $V'(q)$ almost vanishes due to Eq. (33a), so that the behavior of any orbit in the region is of a free motion, as shown in Fig. 7(c) (the dynamics of f is shown there, and that of f^{-1} is basically the same). When $u\ll -1$, a small rectangle on the (u,v) coordinate, centered at (u,v) with sides of lengths Δu and Δv, is mapped by the function $V'(q)$ approximately to an annulus on the q plane (with radii $2\gamma k\exp(-2\gamma u)$ and $2\gamma k\exp[-2\gamma(u+\Delta u)]$). Hence when we put a rectangle with $\Delta v=n\pi/\gamma$ on a flat manifold with $p=p_0$, since this Δv is approximately n periods of the phase $B(q)$, the image of the rectangle by f^{-1} looks like an n-fold annulus when projected on the q plane. In order to distinguish each branch of the n-fold annulus, we propose the boundaries of the partition far from the origin as the form $\{(q,p)\in\mathbb{C}^2|v=v_0+n\pi/\gamma\}$, with v_0 and n being a fixed real number and an arbitrary integer, respectively.

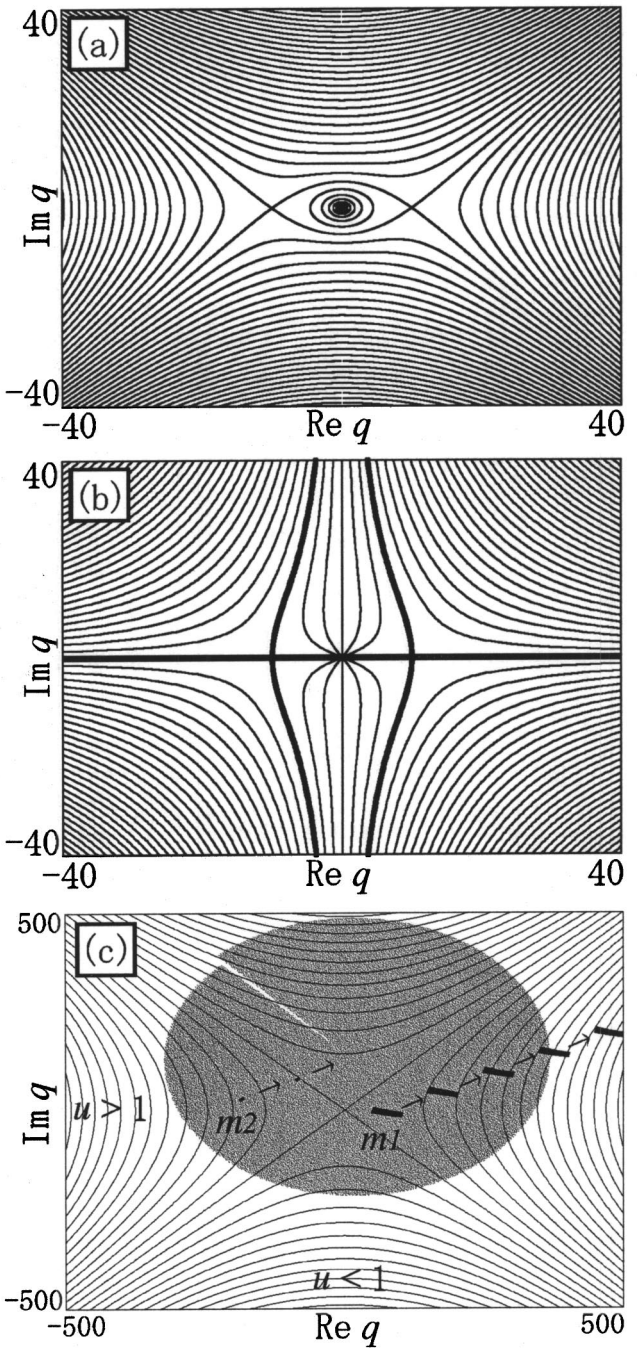

FIG. 7. Contour curves of the functions (a) $A(q)$ and (b) $B(q)$. Each curve is given, in (a), by $A(q)=[1+\ln(2\gamma)]/2+0.4n$ for $n\in\mathbb{Z}$ and, in (b), by $B(q)=\pi n/6$ for $n\in\mathbb{Z}$ with a branch $-\pi\leqslant\arg q<\pi$. Far from $q=0$, these curves are approximated by hyperbolic curves. In (b), a bold part in the side of $\mathrm{Re}\,q>0$ corresponds to the case of $B(q)=0$, and that in the other side corresponds to the cases of $B(q)=-\pi(\mathrm{Im}\,q>0)$ and $\pi(\mathrm{Im}\,q\leqslant 0)$. In these bold parts, the real axis and the others intersect at $q=\pm 1/\sqrt{2\gamma}$. (c) Successive images of small pieces of a flat manifold, $\{(q,p)\in\mathbb{C}^2|p=p_0\}$ with $p_0=100.0+i50.0$, by the map f. Contour curves of the u component of the (u,v) coordinate are superposed. For one of the pieces, m_1, its images are always in a region where $u\gg 1$, so that their behavior is of a free motion. For the other one, m_2, its images expand over a wide range of phase space (a hatched region), as soon as they enter a region where $u\ll 1$.

Around the origin, we estimate the locations of the boundaries by considering a set of real-domain folding points of the flat manifolds, created by f^{-1}. For a flat manifold with $p=p_0\in\mathbb{R}$, we define a folding point on the manifold (q,p_0) by the condition $dp_{-1}(q)/dq=0$, where p_{-1} is the p component of $f^{-1}(q,p_0)$. For p_0 ranging from $-\infty$ to $+\infty$, a set of folding points is obtained as two lines, $\{(q,p)\in\mathbb{R}^2|q=\pm 1/\sqrt{2\gamma}\}$. Hence the boundaries of the partition in complex domain are expected to intersect the real domain around these lines.

We propose a partition of phase space which satisfies the rough estimations presented above both in complex and real domains. To this end, we use the notations

$$U(x,y)=\{(q,p)\in\mathbb{C}^2|x\,\mathrm{Re}\,q>0,\ y\,\mathrm{Im}\,q>0\},\quad (34a)$$

$$\beta(x,y,\nu)=[2\nu xy-(3x+1)y/2]\pi,\quad (34b)$$

where (x,y,ν) is an element of $\mathcal{T}$ defined in Eq. (20). $U(x,y)$ covers a single quadrant of the q plane and $\beta(x,y,\nu)$ always takes an integer times π. For $(x,y,\nu)\in\mathcal{T}$, a phase-space component $U(x,y,\nu)$ is defined by

$$U(x,y,\nu)=\{(q,p)|(q,p)\in U(x,y),$$

$$[B(q)-\beta(x,y,\nu)][B(q)-\beta(x,y,\nu+1)]\leqslant 0\}\quad (35)$$

and, for $(x,y,\nu)=(0,0,0)$, by

$$U(x,y,\nu)=\mathbb{C}^2-\bigcup_{(x',y',\nu')\in\mathcal{T}}U(x',y',\nu').\quad (36)$$

Then our partition $\mathcal{P}$ is defined as a set of the above phase-space components [see Eq. (19) for the definition of boundaries]. Such definition of partition satisfies our rough estimation for the locations of the boundaries. In fact, in the complex domain far from the origin, due to Eqs. (33), the relation $B(q)=\beta(x,y,\nu)$ leads to $v\approx v_0+n\pi/\gamma$ when we set $v_0=-(3x+1)y\pi/4\gamma$ and $n=\nu xy$. Moreover, Fig. 7(b) shows that the boundaries of $\mathcal{P}$ indicated by $B(q)=\beta(x,y,\nu)$ for $x,y\in\{+1,-1\}$ and $\nu=1$ intersect the real phase space at $q=\pm 1/\sqrt{2\gamma}$.

B. Properties of homoclinic orbits

By the partition constructed above, homoclinic points are encoded into symbolic sequences of form (22). In order to estimate imaginary parts of actions, it is necessary to understand typical behaviors exhibited by the homoclinic orbits. Here we present such typical behaviors as two observations obtained from numerical computations. The first observation is concerned with the relation between ν, which is a member of the symbol (x,y,ν), and the flipping amplitude of the corresponding trajectory. The other one is concerned with the relation between the length of a consecutive part $bb\ldots b(b\in\mathcal{S})$ in a symbolic sequence and the behavior of the corresponding trajectory. These are numerical observations and we have no mathematical proof, but the phase-space itinerary of any homoclinic orbit can be well explained by the combinations of the behaviors presented in these observations.

Before presenting the observations, we estimate the locations of homoclinic points in phase space by considering single-step folding processes of flat manifolds. Let m_i and m_f be complex planes defined by $p=p_i$ and $p=p_f$ $(p_i,p_f\in\mathbb{C})$, respectively. The intersection $f(m_i)\cap m_f$ is given by $\{(q,p_f)\in\mathbb{C}^2|A(q)=-\ln|c|,B(q)=-\arg c \pm 2\nu\pi,\nu=0,1,2,\ldots\}$, where $A(q)$ and $B(q)$ are the functions appearing in Eqs. (33), and $c=(p_f-p_i)/(2\gamma k)$. Since the q components of the intersection points are located on a contour curve of $A(q)$, they are located along the axes $\mathrm{Re}\,q=\pm\mathrm{Im}\,q$ asymptotically as $\nu\to+\infty$. Also, as will be seen, the q components of homoclinic points are located along these axes asymptotically as $\nu\to+\infty$, where ν is a member of the symbol (x,y,ν).

Observation 1. Let $\{w_1,w_2,w_3,\ldots\}$ be a set of homoclinic points whose symbolic sequences take the forms

$$\begin{aligned}
&\ldots a_{-2}a_{-1}.b_1a_1a_2\ldots \quad \text{for } w_1,\\
&\ldots a_{-2}a_{-1}.b_2a_1a_2\ldots \quad \text{for } w_2,\\
&\ldots a_{-2}a_{-1}.b_3a_1a_2\ldots \quad \text{for } w_3,\\
&\qquad\vdots
\end{aligned} \tag{37}$$

where a_k for $k\neq0$ is a member of $\mathcal{S}$ defined in Eq. (21), and b_ν for $\nu\in\mathbb{N}$ is given by (x,y,ν), with x and y being fixed members of $\{+1,-1\}$. Then the following relations hold:

$$\lim_{\nu\to+\infty}\sqrt{\gamma/(\nu\pi)}\,q_0(w_\nu)=(x,y), \tag{38a}$$

$$\lim_{\nu\to+\infty}\sqrt{\gamma/(\nu\pi)}\,p_0(w_\nu)=-(x,y), \tag{38b}$$

$$\lim_{\nu\to+\infty}\sqrt{\gamma/(\nu\pi)}\,p_{-1}(w_\nu)=(x,y), \tag{38c}$$

where (q_0,p_0) is the current location of w_ν in phase space and p_{-1} is the momentum at the last time step. The rhs of each equation denotes a pair of signs of real and imaginary parts.

Figure 8 shows the trajectories of w_ν's for small ν's. In the figure, one can see two facts: First, the signs of $\mathrm{Re}\,q_0(w_\nu)$ and $\mathrm{Im}\,q_0(w_\nu)$ are described, respectively, by x and y in the symbol b_ν and second, the amplitudes of $\mathrm{Re}\,q_0(w_\nu)$ and $\mathrm{Im}\,q_0(w_\nu)$ increase with ν much faster than the amplitudes at the other time steps. Due to the second fact, the following approximations hold for large ν's:

$$p_0=q_1-q_0\approx-q_0, \tag{39a}$$

$$p_{-1}=q_0-q_{-1}\approx q_0, \tag{39b}$$

so that the sign of $\mathrm{Re}\,p_0(w_\nu)$ $[\mathrm{Im}\,p_0(w_\nu)]$ is opposite to that of $\mathrm{Re}\,p_{-1}(w_\nu)$ $[\mathrm{Im}\,p_{-1}(w_\nu)]$ for large ν's. Figures 9(a)–9(c), show $q_0(w_\nu)$, $p_0(w_\nu)$, and $p_{-1}(w_\nu)$ for much larger ν's. The magnitudes of the real and imaginary parts of these quantities are shown to have the dependence of the form $\sqrt{\nu\pi/\gamma}$ for sufficiently large ν's. In Fig. 9(d), it is shown that $q_0(w_j)$ diverges much faster than $q_{-1}(w_j)$ and $q_{-2}(w_j)$.

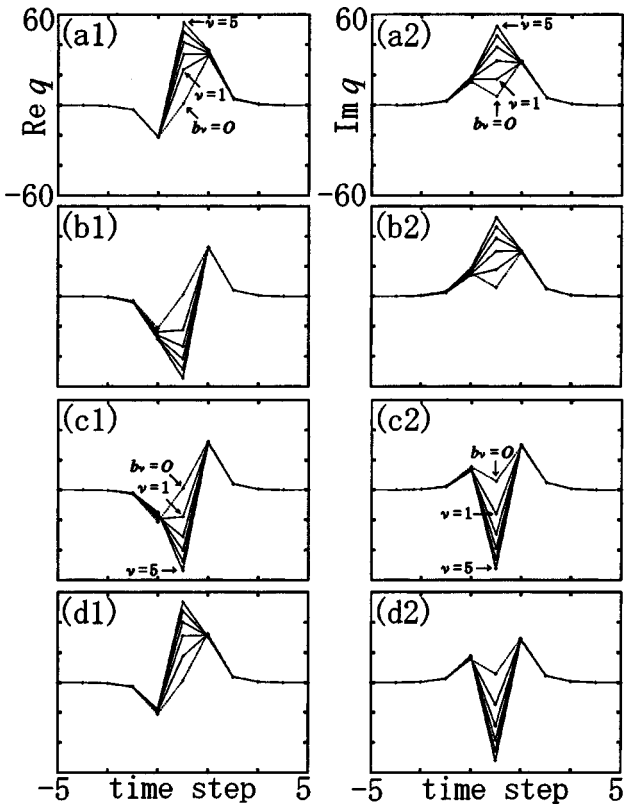

FIG. 8. The trajectories of homoclinic points w_ν's for $\nu=1,2,\ldots,5$. The left and right columns display the real and imaginary parts of the trajectories, respectively. Axes in (a)–(d) have the same scale. The symbolic sequences of w_ν's take the form $\ldots O\,O\,(-1,1,1).b_\nu(1,1,2)\,O\,O\,O\ldots$, where b_ν's are given by (a) $(1,1,\nu)$, (b) $(-1,1,\nu)$, (c) $(-1,-1,\nu)$, and (d) $(1,-1,\nu)$. The dotted lines represent the case that $b_\nu=O$.

Similarly, $q_0(w_j)$ diverges much faster than $q_k(w_j)$ for any other $k\neq0$, though not displayed here.

Relation (38a) leads to

$$\lim_{\nu\to+\infty}|\mathrm{Re}\,q_0(w_\nu)/\mathrm{Im}\,q_0(w_\nu)|=1. \tag{40}$$

In the following, we explain that the relations in Eq. (38) follow, assuming that relation (40) holds for the homoclinic points given by Eqs. (37), and that $q_0(w_\nu)$ diverges much faster than $q_k(w_\nu)$ for any $k\neq0$ as $\nu\to+\infty$.

Relation (38a) is explained as follows. Since $b_\nu=(x,y,\nu)$, w_ν is included in a phase space component $U(x,y,\nu)$ defined in Eq. (35). Then the v component of $q_0(w_\nu)$ in the (u,v) coordinate (32) diverges as $\nu\to+\infty$, since $B(q_0(w_\nu))$ diverges as $\nu\to+\infty$ due to Eq. (19), and $v\approx B(q_0(w_\nu))/(2\gamma)\approx2\nu xy\pi/(2\gamma)$ for large ν's due to Eqs. (33) and (19). Therefore from Eq. (40) and the relation $(\mathrm{Re}\,q_0)(\mathrm{Im}\,q_0)=v\approx\nu xy\pi/\gamma$, we obtain $q_0(w_\nu)\approx\sqrt{\nu\pi/\gamma}\,(x,y)$ for large ν's.

Relation (38c) is explained as follows. The classical equations of motions in Eq. (2) lead to the relation

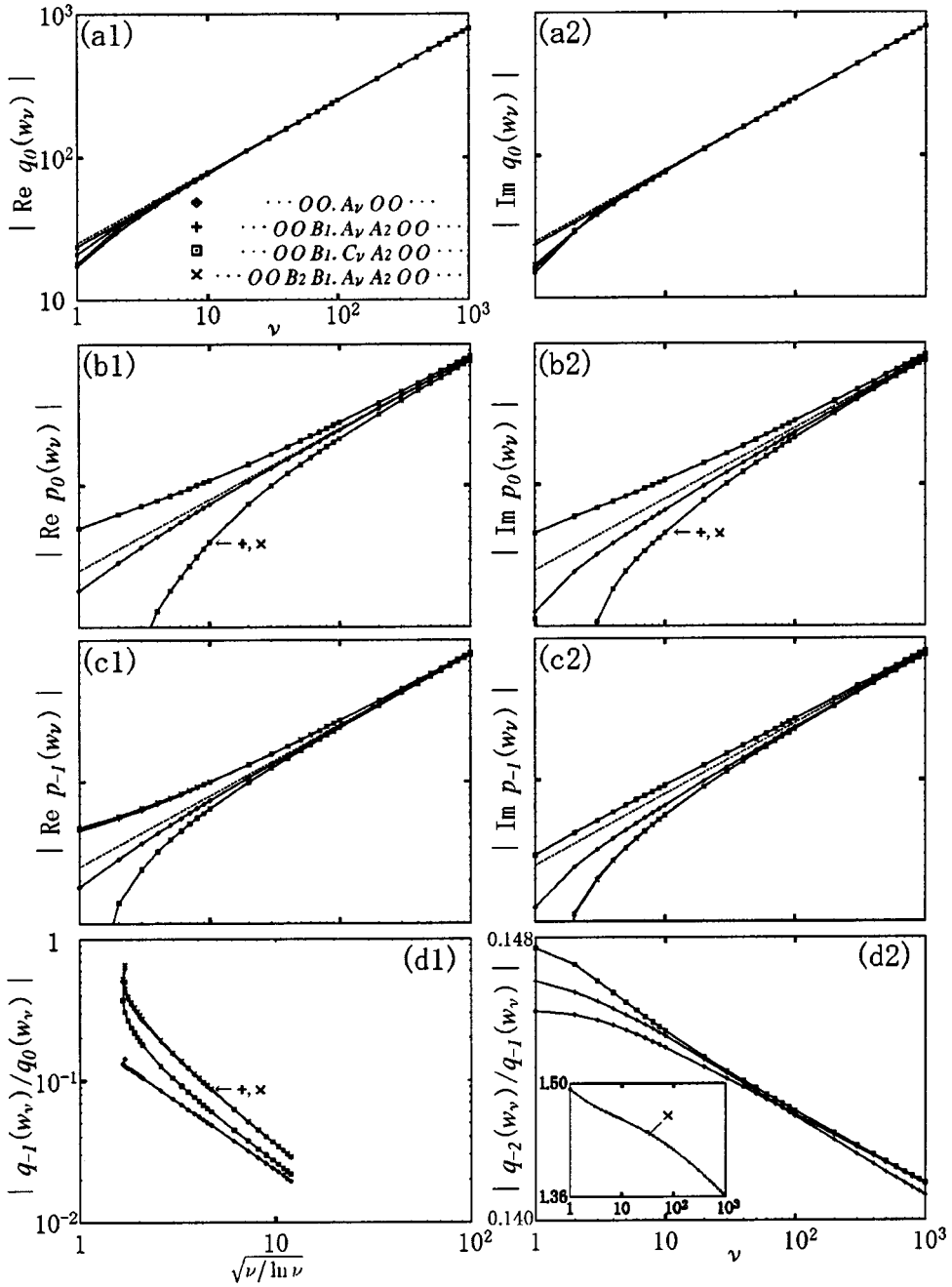

FIG. 9. The dependences of (a) $q_0(w_\nu)$, (b) $p_0(w_\nu)$, (c) $p_{-1}(w_\nu)$, and (d) $|q_{k-1}(w_\nu)/q_k(w_\nu)|$ for $k=0,-1$, on the subscript number ν. Axes in (a)–(c) have the same scale. The symbolic sequences of w_ν's are given in (a), where A_ν, B_ν, and C_ν denote $(1,1,\nu),(-1,1,\nu)$, and $(-1,-1,\nu)$ respectively. The dotted lines in (a)–(c) represent $\sqrt{\nu\pi/\gamma}$. In (a), all curves almost coincide.

$$q_0(w_\nu)+q_{-2}(w_\nu)=2q_{-1}(w_\nu)-V'(q_{-1}(w_\nu)). \quad (41)$$

Since $q_0(w_\nu)$ diverges much faster than $q_{-2}(w_\nu)$ as $\nu\to+\infty$ due to our assumption, the rhs of the above relation diverges in this limit. It means that $q_{-1}(w_\nu)$ also diverges as $\nu\to+\infty$, since the rhs of the relation is an entire function of q_{-1}. In particular, the u component of $q_{-1}(w_\nu)$ diverges as $\nu\to+\infty$, since $(q_{-1}(w_\nu),p_{-1}(w_\nu))$ is always included in the phase-space component $U(a_{-1})$ irrespective of ν. Furthermore, the u component diverges to $-\infty$, since if it diverges to $+\infty$ with $(q_{-1}(w_\nu),p_{-1}(w_\nu))$ being in $U(a_{-1})$, then $\mathrm{Im}\,q_{-1}(w_\nu)$ and $V'(q_{-1}(w_\nu))$ vanish, so that $\mathrm{Im}[q_0(w_\nu)+q_{-2}(w_\nu)]=\mathrm{Im}[2q_{-1}(w_\nu)-V'(q_{-1}(w_\nu))]\to 0$. However, this contradicts that as $\nu\to+\infty$, $|\mathrm{Im}[q_0(w_\nu)+q_{-2}(w_\nu)]|\approx|\mathrm{Im}\,q_0(w_\nu)|\approx\sqrt{\nu\pi/\gamma}\to+\infty$. Thus the u component of $q_{-1}(w_\nu)$ diverges to $-\infty$ as $\nu\to+\infty$. When the u component of $q_{-1}(w_\nu)$ is negatively large, $V'(q_{-1}(w_\nu))$ is exponentially larger than $q_{-1}(w_\nu)$, so that $q_0(w_\nu)\approx -V'(q_{-1}(w_\nu))$. This relation means that $|q_{-1}|\approx\sqrt{\gamma^{-1}\ln|q_0|}$, and thus $p_{-1}(w_\nu)$ has the same dependence as $q_0(w_\nu)$ on ν due to the relation $p_{-1}=q_0-q_{-1}$.

Relation (38b) is explained in a similar way by considering relations $p_0=q_1-q_0$ and Eq. (41) for q_0, q_1, and q_2.

We proceed to the next observation. In usual symbolic dynamics, a consecutive part $b\,b\ldots b$ in a symbolic sequence always corresponds to a fixed point in phase space or the motion approaching the fixed point. However, our classical dynamics always has only a single fixed point at the origin for any choice of positive parameters k and γ, which is easily checked by solving $f(q,p)=(q,p)$, so that the phase-space motion corresponding to a consecutive part $b\,b\ldots b$ with $b\neq O$ is not obvious. Our second observation says that the phase-space motion corresponding to the above consecutive part has a turning point. It is conjectured that as the length of $b\,b\ldots b$ increases, the location of the turning point diverges, so that the trajectory corresponding to $b\,b\ldots b$ does not approach to any point in phase space in the limit of the length.

Observation 2. Let $\{w_1,w_2,w_3\ldots\}$ be a set of homoclinic points whose symbolic sequences take the forms

$$\begin{aligned}
&\ldots a_{-2}a_{-1}.\,b\,b\,a_0a_1a_2\ldots, \quad \text{for } w_1,\\
&\ldots a_{-2}a_{-1}.\,b\,b\,b\,b\,a_0a_1a_2\ldots \quad \text{for } w_2,\\
&\ldots a_{-2}a_{-1}.\,b\,b\,b\,b\,b\,b\,a_0a_1a_2\ldots \quad \text{for } w_3,\\
&\qquad\vdots
\end{aligned} \tag{42}$$

where $b\neq O$ and the length of $b\,b\ldots b$ for w_j is $2j$ ($j\in\mathbb{N}$). Then the trajectory of w_j corresponding to the consecutive part $b\,b\ldots b$ is included in a phase-space component $U(b)$ and the momentum almost vanishes at time step $j-1$. Moreover, the following inequalities hold:

$$0<\mathrm{Re}\,q_{k-1}(w_j)/\mathrm{Re}\,q_k(w_j)<1 \quad (0<k<j), \tag{43a}$$

$$0<\mathrm{Im}\,q_k(w_j)/\mathrm{Im}\,q_{k-1}(w_j)<1 \quad (0<k<j), \tag{43b}$$

$$0<\mathrm{Re}\,q_k(w_j)/\mathrm{Re}\,q_{k-1}(w_j)<1 \quad (j<k<2j), \tag{43c}$$

$$0<\mathrm{Im}\,q_{k-1}(w_j)/\mathrm{Im}\,q_k(w_j)<1 \quad (j<k<2j). \tag{43d}$$

This observation is exemplified in Fig. 10. In the case where the length of $b\,b\ldots b$ in sequences (42) is given by $2j+1$ for w_j, Eqs. (43a) and (43b) hold in the range of $0<k\leqslant j$, and Eqs. (43c) and (43d) hold in the range of $j<k\leqslant 2j$. In this case, the momentum $p_k(w_j)$ at $k=j$ is quite small, but does not vanish.

We conjecture that the q component of the turning point $q_j(w_j)$ diverges with the length of $b\,b\ldots b$, i.e., the following relation holds:

$$\lim_{j\to+\infty} q_j(w_j)=(x\infty,0), \tag{44}$$

where x has the sign of the infinity, which is given by the member of the symbol $b=(x,y,\nu)$. This conjecture is based on the following observation.

Figure 10(c) shows that as j increases, $V(q_j(w_j))$ is approximated by $\alpha e^{i\theta}j^{-\beta}$ where θ, α, and $\beta(>0)$ are real numbers depending on b. If this approximation holds, solving $V(q_j(w_j))=\alpha e^{i\theta}j^{-\beta}$, one obtains a solution

$$(u_j(w_j),v_j(w_j))=(2\gamma)^{-1}(\beta\ln j-\ln(\alpha/k),-\theta), \tag{45}$$

where $(u_j(w_j),v_j(w_j))$ is the location of $q_j(w_j)$ on the (u,v) coordinate. This solution suggests that $\mathrm{Re}\,q_j(w_j)$ diverges and $\mathrm{Im}\,q_j(w_j)$ vanishes as $j\to+\infty$. Moreover, according to Observation 2, $q_j(w_j)$ and the q component of $U(b)$ are included in the same quadrant of the q plane. Therefore relation (44) is obtained. The justification of this relation needs further investigation of classical dynamics, and we hope to report the result of this issue elsewhere.

We have shown that there are two types of behaviors exhibited by homoclinic orbits. In our numerical computations, the behavior of any homoclinic orbit can be understood by the combinations of only two types of motions, one of which is the flipping motions almost along the axes $\mathrm{Re}\,q=\pm\mathrm{Im}\,q$, and the other of which is the motions almost along the contour curves of the v component in the (u,v) coordinate. Which type of motion occurs in the process from (q_k,p_k) to (q_{k+1},p_{k+1}) along a single homoclinic trajectory depends on whether the neighboring symbols in a symbolic sequence, a_k and a_{k+1}, are different (the former type) or the same (the latter type). The former type of motion is characterized by Observation 1, and the latter one by Observation 2.

C. Evaluation of imaginary parts of actions

The imaginary parts of actions for homoclinic orbits are evaluated from symbolic sequences. We first consider the homoclinic points appearing in Observations 1 and 2, and the estimations of imaginary parts of actions for these cases are presented as Observations 3 and 4, respectively. Then using the latter two observations, we estimate the imaginary part of action for any homoclinic orbit. Observation 3 says that the imaginary part of action diverges linearly as $\nu\to+\infty$, where ν is a member of the symbol (x,y,ν). Observation 4 says that the amount of the imaginary part of action is bounded even if the length of a consecutive part $b\,b\ldots b$ ($b\in\mathcal{S}$) in a symbolic sequence tends to infinity. In particular, we observed that phase-space itineraries described by $b\,b\ldots b$ gain little imaginary parts of actions compared to the other itineraries. This means that the homoclinic orbits appearing in Observation 4 can play a semiclassically significant role. Observations 3 and 4 are also entirely based on our numerical computations and, so far, we have no mathematical proof for these observations.

For any homoclinic point w, we consider $s(w)$ defined in Eq. (24) as the imaginary part of action for the orbit of w. The sum in the rhs of (24) is the long time limit of $\mathrm{Im}\,(S_n-L_0)$ [for the definitions of S_n and L_0, see Eq. (8)] and converges due to the exponential convergence of the orbit to the origin. In the definition of $s(w)$, we only take account of the contributions from the forward trajectories, since semiclassical wave functions in our time-domain approach are determined by them. We do not consider the term L_0, since it depends only on the choice of an incident wave packet, not

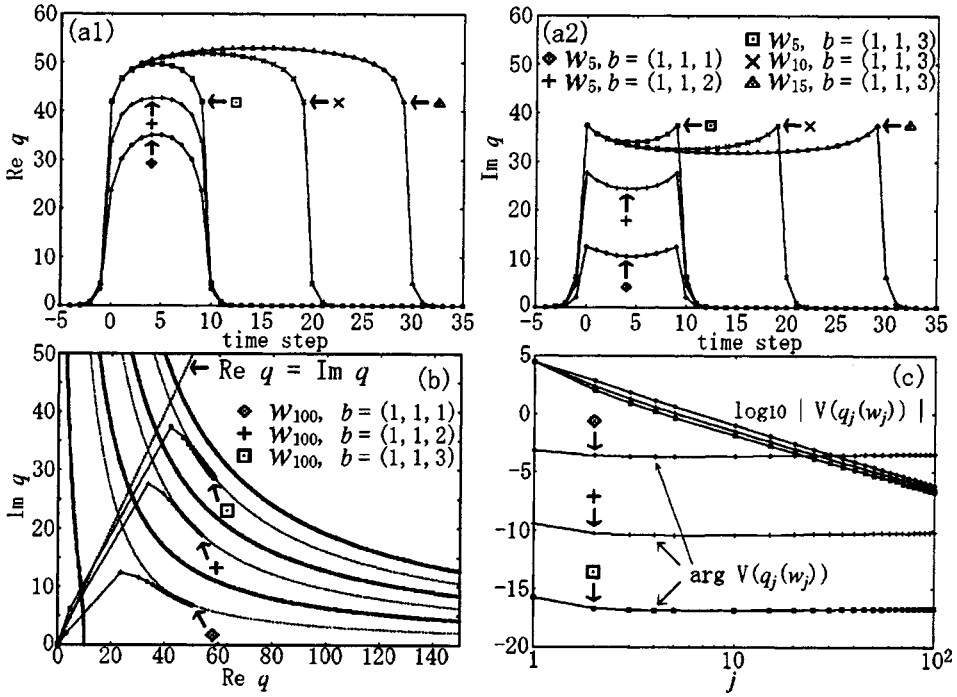

FIG. 10. (a) Trajectories of w_j's for $j=5,10,15$ and (b) for $j=100$. (c) $V(q_j(w_j))$ for j ranging from 1 to 100. The symbolic sequences of w_j's in (a)–(c) take the form $\ldots\ O\,O\,.\,b\,b\ \ldots\ b\,O\,O\ \ldots$, where the length of $b\,b\ldots b$ is $2j$. The types of b used in (a) and in the others are given, respectively, in (a2) and in (b). In (a), amplitudes of $\mathrm{Re}\,p$ and $\mathrm{Im}\,p$ almost vanish at time step $j-1$. In (b), bold curves are the boundaries of our partition. For the discussion in Sec. III C, trajectories for an integrable limit are superposed (dotted curves), which have null energy and connect two infinities of the q plane $(\mathrm{Re}\,q,\mathrm{Im}\,q)=(+\infty,0)$ and $(0,+\infty)$. The dotted line sprouting from the origin represents an axis $\mathrm{Re}\,q=\mathrm{Im}\,q$. In (c), the phase $-2\gamma(\mathrm{Re}\,q_j)(\mathrm{Im}\,q_j)$ is plotted without taking mod 2π.

on classical dynamics. First, we estimate $s(w)$ for the homoclinic points appearing in Observation 1.

Observation 3. Let $\{w_1,w_2,w_3,\ldots\}$ be a set of homoclinic points which appears in Observation 1. Then for any integer $n\geqslant 1$, the following relation holds:

$$\lim_{\nu\to+\infty}[\gamma/(2\nu\pi)]s(f^{-n}(w_\nu))=xy. \tag{46}$$

Figure 11(a) shows the dependence of $|s(f^{-n}(w_\nu))|$ on ν. It can be seen that $|s(f^{-n}(w_\nu))|\approx 2\nu\pi/\gamma$ for large ν's. The condition $n\geqslant 1$ is necessary, since it is essential to relation (46) to take account of the contributions from the flipping motions from $q_{-1}(w_\nu)$ to $q_0(w_\nu)$ displayed in Fig. 8.

In the following, we explain relation (46), assuming that Observation 1 holds, and that for the homoclinic points appearing in Observation 1, $q_k(w_\nu)$ $[q_{-k}(w_\nu)]$ for $k\geqslant 0$ diverges much faster than $q_{k+1}(w_\nu)$ $[q_{-(k+1)}(w_\nu)]$ as $\nu\to+\infty$. Figure 9(d) suggests that the second assumption is valid for $k=0$ and 1. For the other k's, it has not been found numerically whether the assumption is valid or not, since $q_k(w_\nu)$ and $q_{-k}(w_\nu)$ for $k\geqslant 2$ remain to be immediate values even for $\nu\approx 1000$, so that the numerical computation needs too high accuracy to make clear the asymptotic behaviors of $|q_{\pm k}(w_\nu)|$ with sufficiently large magnitudes. However, the exponential dependence of $V'(q)$ on u and v shown in Eqs. (33) means that the large difference in $q_k(w_j)[q_{-k}(w_j)]$ results from the slight difference in $q_{k+1}(w_j)[q_{-(k+1)}(w_j)]$ by the map f^{-1} (f), so that the assumption for $k\geqslant 2$ is expected to be valid.

We first discuss the kinetic part and then the potential part of $s(f^{-n}(w_\nu))$, respectively. In the kinetic part, $\Sigma_{k=-n+1}^{+\infty}\mathrm{Im}\,T(p_{k-1}(w_\nu))$, each term is written as

$$\mathrm{Im}\,T(p_{k-1}(w_\nu))=[\mathrm{Re}\,p_{k-1}(w_\nu)][\mathrm{Im}\,p_{k-1}(w_\nu)]. \tag{47}$$

Due to the assumptions we put, the following inequalities hold for $k\neq 0,-1$ and for large ν's:

$$|\mathrm{Re}\,p_k(w_\nu)|\ll|\mathrm{Re}\,p_{-1}(w_\nu)|,|\mathrm{Re}\,p_0(w_\nu)|, \tag{48a}$$

$$|\mathrm{Im}\,p_k(w_\nu)|\ll|\mathrm{Im}\,p_{-1}(w_\nu)|,|\mathrm{Im}\,p_0(w_\nu)|. \tag{48b}$$

Then the kinetic part of $s(f^{-n}(w_\nu))$ is dominated by the terms $\mathrm{Im}\,T(p_{-1}(w_\nu))$ and $\mathrm{Im}\,T(p_0(w_\nu))$ due to Eq. (47). Since Observation 1 says that the quantities in the rhs of the above inequalities are proportional to $\nu^{1/2}$ for large ν's, $\mathrm{Im}\,T(p_{-1}(w_\nu))$ and $\mathrm{Im}\,T(p_0(w_\nu))$ have linear dependences on large ν's. Hence the kinetic part of $s(f^{-n}(w_\nu))$ is expected to have a linear dependence on large ν's. Figure 11 shows that the kinetic part of $s(f^{-n}(w_\nu))$ is actually dominated by $\mathrm{Im}\,T(p_{-1}(w_\nu))$ and $\mathrm{Im}\,T(p_0(w_\nu))$, and has a linear dependence on large ν's.

In the potential part of $s(f^{-n}(w_\nu))$, i.e., $\Sigma_{k=-n+1}^{+\infty}\mathrm{Im}\,V(q_k(w_\nu))$, each term is written as

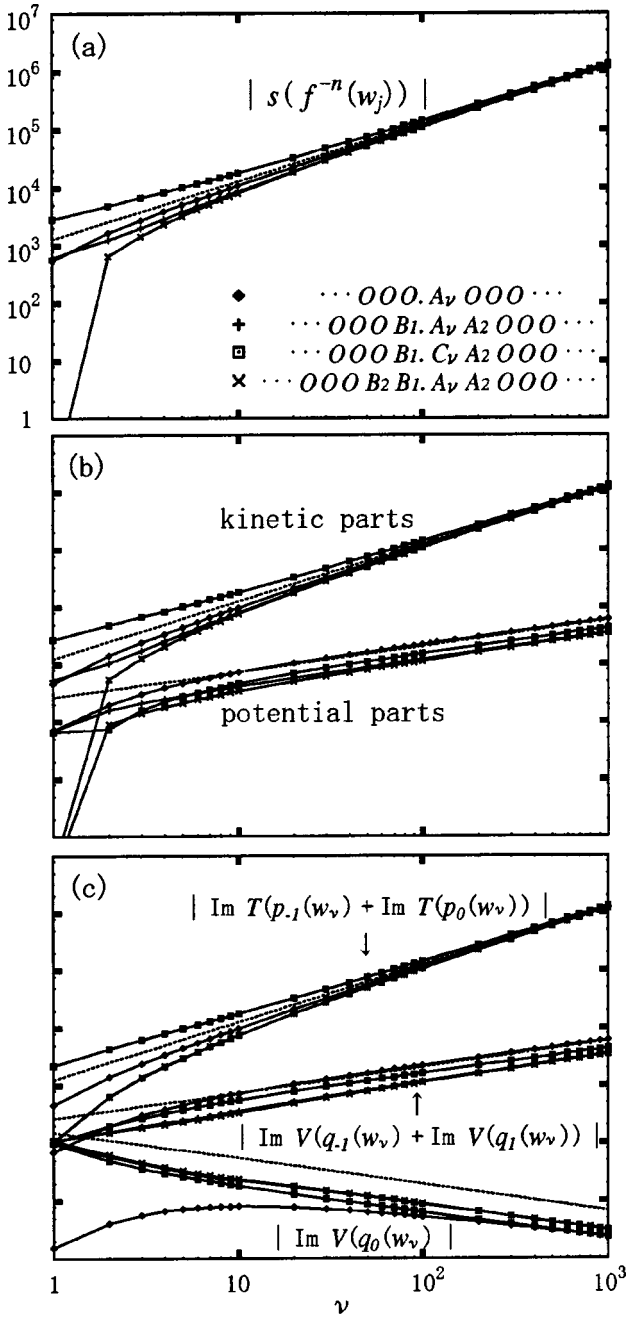

FIG. 11. (a) $|s(f^{-n}(w_\nu))|$ for $n=4$ and $\nu=1$–1000. The symbolic sequences of w_ν's are the same as in Fig. 9. The dotted line represents $2\nu\pi/\gamma$. Axes in (a)–(c) have the same scale. (b) The absolute values of the kinetic parts and the potential ones of $s(f^{-n}(w_\nu))$. The upper dotted line and the lower dotted curve represent $2\nu\pi/\gamma$ and $2g(\sqrt{2\nu\pi/\gamma})$, respectively, where $g(x)=x/(2\sqrt{\gamma \ln x})$. (c) $|\mathrm{Im}\, T(p_{-1}(w_\nu))+\mathrm{Im}\, T(p_0(w_\nu))|$, $|\mathrm{Im}\, V(q_{-1}(w_\nu))+\mathrm{Im}\, V(q_1(w_\nu))|$, and $|\mathrm{Im}\, V(q_0(w_\nu))|$. The top dotted line and middle dotted curve are the same as in (b) and the bottom dotted curve represents $[2\gamma^2 g(\sqrt{2\nu\pi/\gamma})]^{-1}$.

$$\mathrm{Im}\, V(q_k(w_\nu))=\mathrm{Im}\left[\frac{q_{k+1}(w_\nu)-2q_k(w_\nu)+q_{k-1}(w_\nu)}{2\gamma q_k(w_\nu)}\right] \tag{49}$$

by incorporating a relation $p_k=p_{k-1}-V'(q_k)$ given by Eq. (2) and a relation $V'(q)=-2\gamma qV(q)$ satisfied by our $V(q)$. Simple arithmetic of the rhs of Eq. (49) yields the inequality

$$|\mathrm{Im}\, V(q_k(w_\nu))|\leqslant\frac{|q_{k+1}(w_\nu)|+|q_{k-1}(w_\nu)|}{2\gamma|q_k(w_\nu)|}. \tag{50}$$

Based on the assumptions imposed here, we can develop the same argument as that just below Eq. (41) (note that the assumptions here are stronger than those imposed there). As a result, one obtains that $|q_1(w_\nu)|,|q_{-1}(w_\nu)| \approx\sqrt{\gamma^{-1}\ln|q_0(w_\nu)|}$ for large ν's. In a similar way, one obtains that $|q_{\pm(k+1)}(w_\nu)|\approx\sqrt{\gamma^{-1}\ln|q_{\pm k}(w_\nu)|}$ for $k\geqslant 1$ and large ν's. By using these relations, the rhs of Eq. (50) is approximated by

$$[2\gamma^2 g(|q_k(w_\nu)|)]^{-1} \quad \text{for } k=0, \tag{51a}$$

$$g(|q_{k-1}(w_\nu)|) \quad \text{for } k>0, \tag{51b}$$

$$g(|q_{k+1}(w_\nu)|) \quad \text{for } k<0, \tag{51c}$$

where $g(x)=x/(2\sqrt{\gamma \ln x})$. Here we used an approximation $|q|+\sqrt{\gamma^{-1}\ln|q|}\approx|q|$ for large $|q|$.

Since $|q_0(w_\nu)|\approx\sqrt{2\nu\pi/\gamma}$ for large ν's according to Observation 1, the rhs of Eq. (50) is approximated by

$$[2\gamma^2 g(\sqrt{2\nu\pi/\gamma})]^{-1} \quad \text{for } k=0, \tag{52a}$$

$$g(\sqrt{2\nu\pi/\gamma}) \quad \text{for } k=\pm 1, \tag{52b}$$

$$g(\sqrt{\ln'\{\ln'[\ \ldots \ln'(2\pi\nu/\gamma)\ \ldots]\}}) \quad \text{for } |k|\geqslant 2, \tag{52c}$$

where $\ln' x=(2\gamma)^{-1}\ln x$, and the argument of the square root in Eq. (52c) is a $|k|-1$ fold logarithm of $2\pi\nu/\gamma$.

Since $g(x)$ in Eq. (52) is monotonically increasing for large x, one can expect that the potential part of $s(f^{-n}(w_\nu))$ for large ν's is dominated by the terms $\mathrm{Im}\, V(q_{-1}(w_\nu))$ and $\mathrm{Im}\, V(q_1(w_\nu))$. More precisely, from Eq. (52b), the potential part of $s(f^{-n}(w_\nu))$ is expected to be approximated by $2g(\sqrt{2\nu\pi/\gamma})$ for large ν's. Also, from Eq. (52a), $\mathrm{Im}\, V(q_0(w_\nu))$ is expected to vanish as $\nu\rightarrow+\infty$. Figure 11 shows that the potential part of $s(f^{-n}(w_\nu))$ is actually dominated by the terms $\mathrm{Im}\, V(q_{-1}(w_\nu))$ and $\mathrm{Im}\, V(q_1(w_\nu))$ for large ν's, and the asymptotic behavior of the potential part for large ν's is described by $2g(\sqrt{2\nu\pi/\gamma})$. It is also shown that $\mathrm{Im}\, V(q_0(w_\nu))$ tends to vanish as ν increases.

Since the ratios of the terms in Eq. (52) to ν vanish as $\nu\rightarrow+\infty$, $s(f^{-n}(w_\nu))$ for large ν's is dominated by the kinetic part. Therefore the following estimation is finally obtained for large ν's:

$$\begin{aligned} s(f^{-n}(w_\nu))&\approx\mathrm{Im}T(p_{-1}(w_\nu))+\mathrm{Im}\, T(p_0(w_\nu))\\ &=[\mathrm{Re}\, p_{-1}(w_\nu)][\mathrm{Im}\, p_{-1}(w_\nu)]+[\mathrm{Re}\, p_0(w_\nu)]\\ &\quad\times[\mathrm{Im}\, p_0(w_\nu)]\\ &\approx(2\nu\pi/\gamma)xy. \end{aligned} \tag{53}$$

In the last approximation, the relations in Eq. (38) are used.

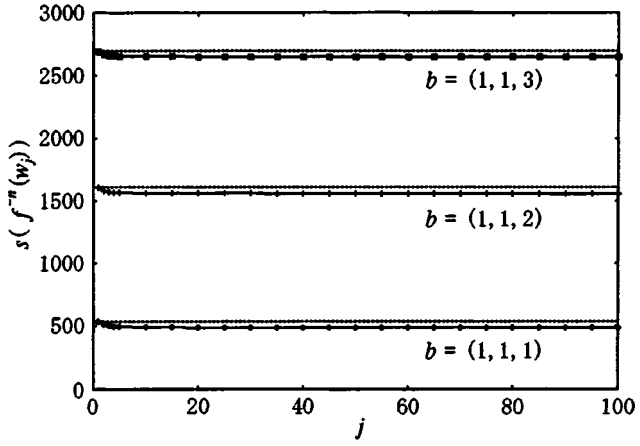

FIG. 12. $s(f^{-n}(w_j))$ for $n=4$ and $j=1-100$. The symbolic sequences of w_j's are the same as in Fig. 10(b). Solid lines indicate $s(f^{-n}(w))$ for w's which have sequences of form (55).

Next we estimate $s(w)$ for the homoclinic points appearing in the Observation 2.

Observation 4. Let $\{w_1,w_2,w_3,\ldots\}$ be a set of homoclinic points which appears in Observation 2. Then for any integer n, the following sequence is bounded:

$$s(f^{-n}(w_1))s(f^{-n}(w_2))s(f^{-n}(w_3))\ldots. \tag{54}$$

Figure 12 shows the dependence of $s(f^{-n}(w_j))$ on j. In the case of this figure, sequence (54) does not deviate largely from $s(f^{-n}(w))$ for a homoclinic point w which has the symbolic sequence

$$\ldots O\,O\,.\,b\,O\,O\ldots. \tag{55}$$

This means that each element in sequence (54) is dominated by the contributions from the flipping motions between components $U(b)$ and $U(O)$. Though not displayed here, when w_j's have symbolic sequences of the form

$$\ldots a_{-2}\,a_{-1}\,.\,b\,b\ldots b\,a_0\,a_1\ldots, \tag{56}$$

we observed that sequence (54) does not deviate greatly from the action for the case

$$\ldots a_{-2}\,a_{-1}\,.\,b\,a_0\,a_1\ldots. \tag{57}$$

Hence the imaginary parts of actions are mainly gained by phase-space itineraries described by sequences other than $b\,b\ldots b$. This means that itineraries described by $b\,b\ldots b$ can be semiclassically significant in the tunneling processes since smaller imaginary parts of actions yield larger semiclassical amplitudes. As in Observation 2, the same statement as Observation 4 holds when the length of the sequence $b\,b\ldots b$ is given by $2j+1$ for w_j.

We discuss why sequence (54) is bounded. Remembering the discussion leading to conjecture (44), one can see that $H(q_j(w_j),p_{j-1}(w_j))\approx 0$ for $H(q,p)=T(p)+V(q)$ and for large j's, since $T(p_{j-1}(w_j))\approx 0$ due to Observation 2, and $V(q_j(w_j))\approx 0$ [hence $V(q_{j-1}(w_j))\approx 0$] as shown in Fig. 10(c). Figure 10(b) shows homoclinic trajectories of our map and trajectories for the integrable flow Hamiltonian $H(q,p)$ with null energy. It can be seen that the homoclinic trajectories are along the integrable trajectories for the duration of itineraries described by $b\,b\ldots b$. In fact, we observed that $H(q_k(w_j),p_{k-1}(w_j))$ almost vanish for k's corresponding to the duration. Hence the members of sequence (54) can be evaluated by using the integrable trajectories. Since the imaginary parts of actions of the integrable trajectories are bounded (see Appendix C), sequence (54) is expected to be bounded.

By making use of Observations 3 and 4, we estimate $s(w)$ for any homoclinic point w, which has a symbolic sequence of form (22). We denote $a_k=(x_k,y_k,\nu_k)$ for any k and assume that ν_k is large if $a_k\neq O$. Then two cases have to be discussed.

First is the case where the symbolic sequence of w does not include a consecutive part, $b\,b\ldots b$. For any integer k and for $a_k\neq O$, we approximate $q_k(w)$ according to Observation 1 by

$$q_k(w)\approx(\nu_k\pi/\gamma)^{1/2}(x_k,y_k). \tag{58}$$

For $a_k=O$, we approximate $q_k(w)$ by (0,0). This approximation is equivalent to substituting $(x_k,y_k)=(0,0)$ into Eq. (58). From the relation $p_{k-1}=q_k-q_{k-1}$, $p_{k-1}(w)$ is approximated by

$$p_{k-1}(w)\approx(\pi/\gamma)^{1/2}(x_k\nu_k^{1/2}-x_{k-1}\nu_{k-1}^{1/2},y_k\nu_k^{1/2}-y_{k-1}\nu_{k-1}^{1/2}). \tag{59}$$

Then due to Eq. (47), $\mathrm{Im}\,T(p_{k-1}(w))$ is approximated by

$$\mathrm{Im}\,T(p_{k-1}(w))\approx(\pi/\gamma)(x_k\nu_k^{1/2}-x_{k-1}\nu_{k-1}^{1/2})\times(y_k\nu_k^{1/2}-y_{k-1}\nu_{k-1}^{1/2}). \tag{60}$$

Since the imaginary part of action gained at each time step is dominated by the kinetic part, as discussed below Observation 3, $s(w)$ is estimated by the sum over the terms in the rhs of Eq. (60) for $k\geqslant 1$.

The second is the case where the symbolic sequence of w includes a consecutive part, $b\,b\ldots b$. The imaginary part of action gained along the itinerary described by $b\,b\ldots b$ is negligible compared to that along the other part of the trajectory, as discussed below Observation 4. From this fact, we approximate the imaginary part of action for the trajectory of $b\,b\ldots b$ by a null value. This approximation is equivalent to evaluating the imaginary part of action only by its kinetic part and then substituting $(x_{k-1},y_{k-1},\nu_{k-1})=(x_k,y_k,\nu_k)$ into Eq. (60).

As a result, whether a consecutive part $b\,b\ldots b$ is included in the symbolic sequence or not, the imaginary part of action is estimated only by its kinetic part

$$s(w)\approx\sum_{k=1}^{+\infty}\mathrm{Im}\,T(p_{k-1}(w)). \tag{61}$$

Hence substituting Eq. (60) into the rhs of the above, we finally obtain estimation (25).

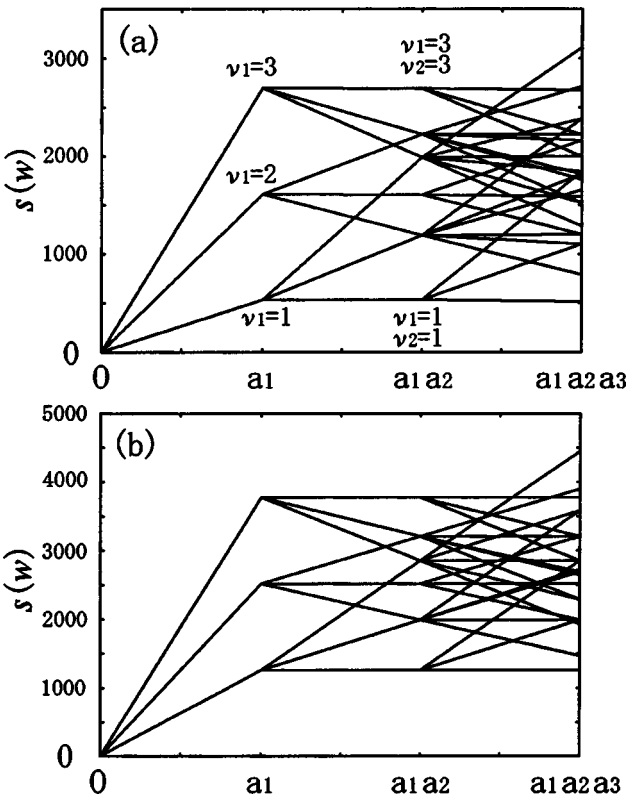

FIG. 13. Imaginary parts of actions evaluated from (a) actual trajectories of homoclinic points and (b) symbolic sequences assigned to the homoclinic points. In each figure, the origin represents a null imaginary part of action gained by the fixed point, $(q,p)=(0,0)$, associated with a symbolic sequence $\ldots O\,O\,.\,O\,O\,O\ldots$. The first to the third columns labeled by a_1, a_1a_2, and $a_1a_2a_3$ show the imaginary parts of actions gained by the trajectories of the homoclinic points associated, respectively, with $\ldots O\,O\,.\,O\,O\,O\,a_1\,O\,O\ldots$, $\ldots O\,O\,.\,O\,O\,O\,a_1\,a_2\,O\,O\ldots$, and $\ldots O\,O\,.\,O\,O\,O\,a_1\,a_2\,a_3\,O\,O\ldots$, where $a_1,a_2,a_3 \in\{(1,1,\nu)|\,\nu=1,2,3\}$.

Figure 13 shows the imaginary parts of actions evaluated from actual trajectories of homoclinic points and from symbolic sequences assigned to the homoclinic points. Estimation (61) is based on the assumption that ν_k is large if $a_k \neq O$, however, as shown in the figure, the estimation is still valid for small ν_k's. This is because the approximation in Eq. (58) is not so crude for small ν_k's, as is shown in Fig. 9(a).

In each column of Fig. 13(a), the smallest $s(w)$ is associated with a symbolic sequence $\ldots O\,O\,.\,O\,O\ldots$ or $\ldots O\,O\,.\,O\,O\,O\,b\,b\ldots b\,O\,O\ldots$ with $b=(1,1,1)$. Appendix B shows such types of symbolic sequences, including the case where $b=(-1,-1,1)$, attain the smallest $s(w)$ in the whole candidates. In Sec. II F, we evaluated the tunneling wave functions by the semiclassical candidate orbits described by these types of sequences, typical behavior of which was illustrated in Fig. 5(c).

IV. CONCLUSION AND DISCUSSION

A. Conclusion

We have carried out complex semiclassical analysis for the tunneling problem of a kicked scattering model which creates chaotic dynamics in complex domain. Although classical motions in real phase space are simple, tunneling wave functions exhibit a complicated pattern, which is typically observed in chaotic systems. The wave functions were reproduced semiclassically in excellent agreement with fully quantum calculations. It enables us to interpret the creation of the complicated pattern appearing in the tunneling regime. Complex orbits contributing to the semiclassical wave functions are embedded in the hierarchical structure of initial-value sets. The hierarchical structure is a reflection of the emergence of a homoclinic tangle in complex phase-space, i.e., the manifestation of complex-domain chaos, and provides the mechanism: the interferences of orbits over generations. On the basis of symbolic dynamics constructed in the complex domain, phase-space itineraries of tunneling orbits were related with the amounts of imaginary parts of actions gained by the orbits. Incorporation of symbolic dynamics with the complex semiclassical method has enabled us to discuss quantitatively the competition among tunneling orbits and has elucidated the significant role of complex-domain chaos in the tunneling processes of nonintegrable systems.

B. Chaotic tunneling

We further discuss the role of complex-domain chaos played in the semiclassical description of tunneling processes in nonintegrable systems. In the present study, we adopted a time-domain approach of the complex semiclassical method. This approach is concerned with the real-time classical propagation and has nothing to do with the instanton processes. This means that real-domain paths are not connected to complex-domain paths, in other words, both the real domain and the other domain are invariant under the classical dynamics. Therefore all candidate orbits to describe tunneling processes are always exposed to complex-domain chaos, not to real-domain one. In this sense, it is natural to consider the role of the complex-domain chaos in our approach.

In our semiclassical framework, initial and final quantum states are identified with classical manifolds in complex phase space. The evolution of the manifolds is involved in the stretching and folding dynamics in the complex domain. The hierarchical arrangements of initial values which we observed is nothing but the structure of the section of one backward evolved manifold $f^{-n}(\mathcal{F})$ cut by the other manifold $\mathcal{I}$. Our result here strongly suggests that the creation of the hierarchical structure of initial-value sets is only due to the emergence of complex-domain chaos, irrespective of the existence of real-domain chaos and also irrespective of the types of tunneling, i.e., whether energy-barrier tunneling or dynamical one [28].

The chaotic dynamics in phase space is created on the Julia set, which includes the complex homoclinic tangle investigated here. The trajectories in this set are proved to be sufficient to describe tunneling in the case of the complex Hénon map [18]. It was numerically confirmed here that this statement is correct also in our case. Therefore, on the basis of our present study and Ref. [18], we would like to present the notion of ''chaotic tunneling,'' which first appeared in

Ref. [5], as the tunneling in the presence of the Julia set.

In energy-domain approaches [6,7,13,14], to the best of our knowledge, the complex-domain chaos has not been used explicitly in semiclassical calculations. The significant role of the complex domain chaos played in the time-domain approach should have the correspondence in the energy-domain ones. However, the instanton concept, which is intrinsic to these approaches, makes it difficult to see such correspondence. The reason is that even when one takes full account of complex classical dynamics, the degree of freedom of the path deformation on the complex time plane often allows one to consider complicated classical processes in complex domain as the composition of real-domain chaotic processes and instantonlike ones [7,13]. The authors of Ref. [13] have reported complicated patterns of stationary wave functions and explained them in terms of stable and unstable manifolds. This implies that both manifolds are the key objects to relate time-domain and energy-domain approaches. We would like to describe the tunneling phenomena in nonintegrable systems in terms of the simple notion, chaotic tunneling. Therefore the role of complex-domain chaos in the energy-domain approaches is desired to be clarified in further studies.

C. Discussion

Finally, we itemize several future problems to make our theory more self-contained, given as follows.

(1) We have constructed a partition of phase space in terms of the phase part of the gradient of a potential function. A similar approach can be found in the context of the study on a dynamical system of an exponential map of one complex variable [29], where the boundaries of a partition correspond to the contour curves of the phase part of the exponential function. Genericness of our approach should be examined in further studies.

(2) Reproducing tunneling wave functions, we did not enter into details of the treatment of the Stokes phenomenon. Empirically, symbolic sequences which include members of the form $(1,-1,\nu)$ or $(-1,1,\nu)$ with $\nu \in \mathbb{N}$ should be excluded from the whole candidates. In particular, according to such empirical rule, we have excluded from the candidates those trajectories which have almost null imaginary parts of actions due to the cancellation between the imaginary parts gained at individual time steps. When the condition $q_{n+k} = q^*_{n-k-1}$ is satisfied for any $k \geqslant 0$ with n being fixed, where the asterisk denotes the complex conjugate, the imaginary parts of actions integrated over the whole time axis become null. We observed numerically that such condition is satisfied by the symbolic sequences of homoclinic points such that the relation between symbols, $(x_{n+k}, y_{n+k}, \nu_{n+k}) = (x_{n-k-1}, -y_{n-k-1}, \nu_{n-k-1})$, holds for any $k \geqslant 0$ with n being fixed. In fact, there is an infinite number of symbolic sequences satisfying such relation. The criterion for whether tunneling orbits well approximated by the homoclinic orbits described by such symbolic sequences are semiclassically contributable or not would be beyond our intuitive expectation based on the amount of imaginary parts of actions [25]. The criterion should be given only by a rigorous treatment of the Stokes phenomenon. The justification of our empirical rule mentioned above needs the consideration of the intersection problem of the Stokes curves, and we are now investigating this issue.

(3) In many nonintegrable open systems with the condition that $V'(q) \to 0$ as $|q| \to +\infty$, real-domain trajectories which diverge to infinity are indifferent, i.e., have null Lyapunov exponents, in contrast to the case of open systems with polynomial potential functions. Because of that, in the former systems, generic properties of complex trajectories exploring in the vicinity of real-domain asymptotic region are not obvious, in spite of their semiclassical significant role as has been seen in our present study. The result of the investigation of this issue will be reported elsewhere.

ACKNOWLEDGMENT

One of the authors (T.O.) is grateful to A. Tanaka for stimulating discussions.

APPENDIX A: NO CHAOTIC MOTION FOUND IN REAL DOMAIN

We prove that Eq. (2) has no chaotic solution in $\mathbb{R}^2$ when $V(q)$ is unimodal, i.e., $-V'(q) > 0, < 0$, and $= 0$ for $q > 0$, < 0,and$= 0$, respectively. More precise statement is that for unimodal $V(q)$ and any $(q,p) \in \mathbb{R}^2$, if the forward (backward) orbit of (q,p) is bounded, then the forward (backward) orbit is either fixed at (0,0) or approaching (0,0).

First, it is shown that any point except (0,0) diverges by forward or backward iterations of the map f. It is trivial that $(q,p) = (0,0)$ is a solution of Eq. (2). Assume that a solution, $\{(q_j, p_j) | j \in \mathbb{Z}\}$, satisfies $q_0 p_0 > 0$. A relation $q_1 = q_0 + p_0$ immediately leads us to $q_0 q_1 > 0$ and $|q_1| > |q_0|$. Another relation $p_1 = p_0 - V'(q_1)$ and the unimodality condition $-q_1 V'(q_1) > 0$ for $q_1 \neq 0$ lead us to $p_0 p_1 > 0$ and $|p_1| > |p_0|$. Then applying the discussion recursively, we obtain that $|q_j| (= |q_0 + p_0 + \cdots + p_{j-1}|)$ diverges as $j \to +\infty$. In a similar way, in the case that $q_0 p_0 < 0$, we obtain that $|q_{-j}| (= |q_0 - p_{-1} - \cdots - p_{-j}|)$ diverges as $j \to +\infty$, though one has to solve Eq. (2) backwardly. When $q_0 p_0 = 0$ and $(q_0, p_0) \neq (0,0)$, either $q_1 p_1 \neq 0$ or $q_{-1} p_{-1} \neq 0$ holds, so that the same discussion can be applied.

Second, it is shown that for any point except (0,0), if its forward or backward orbit is bounded, then the orbit approaches (0,0). We only prove the case of forwardly bounded orbits, since the case of backwardly bounded ones is straightforward. Assume that a forward trajectory, $\{(q_j, p_j) | j \in \mathbb{N}\}$, is included in B, a compact set in $\mathbb{R}^2$. Then there exists an accumulation value (q_*, p_*) in B for the trajectory. By definition, $f^j(q_*, p_*)$ for any $j \in \mathbb{Z}$ is also an accumulation value. Since $\{(q_j, p_j) | j \in \mathbb{N}\} \subset B$, we obtain that $\{f^j(q_*, p_*) | j \in \mathbb{Z}\} \subset B$. Any orbit both forwardly and backwardly bounded must be (0,0) due to our former discussion. Hence the fixed point (0,0) is the only accumulation value, so that the orbit of (q_0, p_0) approaches (0,0). So the statement has been proved.

APPENDIX B: ORDER OF SYMBOLIC SEQUENCES

Here the order of symbolic sequences is given according to the amounts of imaginary parts of actions estimated by Eq. (25). Let us consider a set of symbolic sequences Σ:

$$\Sigma=\{a_0\,a_1\ldots a_n\,O\,O\ldots|n\geqslant 0,a_k\in\mathcal{S}',k\geqslant 0\}, \tag{B1a}$$

$$\mathcal{S}'=\{(1,1,\nu),(-1,-1,\nu)|\,\nu\in\mathbb{N}\}\cup\{O\}. \tag{B1b}$$

For any $\sigma,\sigma'\in\Sigma$, we define an equivalent relation by

$$\sigma\sim\sigma'\Leftrightarrow\tilde{s}(\sigma)=\tilde{s}(\sigma'), \tag{B2}$$

where $\tilde{s}(\sigma)$ denotes the value of the rhs of Eq (25) evaluated for σ. For any two members of $\Sigma/\sim$, $[\sigma]$ and $[\sigma']$, the order between them is defined by

$$[\sigma]<[\sigma']\Leftrightarrow\tilde{s}(\sigma)<\tilde{s}(\sigma'). \tag{B3}$$

It is easily checked that $\tilde{s}(\sigma)\geqslant 0$ for any $\sigma\in\Sigma$ and the equality holds if and only if $\sigma=O\,O\,O\ldots$. Then one obtains

$$[O\,O\,O\ldots]<[\sigma]\Leftrightarrow\sigma\neq O\,O\,O\ldots. \tag{B4}$$

For any $[\sigma]$ except $[O\,O\,O\ldots]$, the representative σ can be chosen such that

$$\sigma=a_0\,a_1\ldots a_n\,O\,O\ldots\quad(n\geqslant 0), \tag{B5a}$$

$$a_n\neq O,\quad a_{k-1}\neq a_k\quad(1\leqslant k\leqslant n). \tag{B5b}$$

For σ in Eq. (B5), the following relations hold:

$$\begin{aligned}[a_n\,O\,O\ldots]&<[a_{n-1}\,a_n\,O\,O\ldots]\\&<\ldots\ldots\\&<[a_0\,a_1\ldots a_n\,O\,O\ldots]=[\sigma].\end{aligned} \tag{B6}$$

Since, for any $\nu\in\mathbb{N}$,

$$\begin{aligned}\tilde{s}((1,1,\nu)\,O\,O\ldots)&=\tilde{s}((-1,-1,\nu)\,O\,O\ldots)\\&<\tilde{s}((-1,-1,\nu+1)\,O\,O\ldots)\\&=\tilde{s}((1,1,\nu+1)\,O\,O\ldots),\end{aligned} \tag{B7}$$

one of the following relations holds:

$$[(1,1,1)\,O\,O\ldots]<[\sigma], \tag{B8a}$$

$$[(1,1,1)\,O\,O\ldots]=[\sigma]. \tag{B8b}$$

Finally, from Eqs. (B4) and (B8), one obtains the relations

$$[O\,O\,O\ldots]<[(1,1,1)\,O\,O\ldots]<[\sigma] \tag{B9}$$

for any $[\sigma]$ except $[O\,O\,O\ldots]$ and $[(1,1,1)\,O\,O\ldots]$. It is not difficult to check that $[(1,1,1)\,O\,O\ldots]$ is equal to

$$\{b\,b\ldots b\,O\,O\ldots\,|\,b=(1,1,1)\ \text{ or }\ (-1,-1,1)\}. \tag{B10}$$

APPENDIX C: IMAGINARY PARTS OF ACTIONS FOR INTEGRABLE TRAJECTORIES

We consider a Hamiltonian $H(q,p)=T(p)+V(q)$ with $T(p)=p^2/2$ and $V(q)=k\exp(-\gamma q^2)$, and evaluate the imaginary parts of actions for the trajectories which satisfy $H(q,p)=0$ and connect two infinities of the q plane $(\mathrm{Re}\,q,\mathrm{Im}\,q)=(+\infty,0)$ and $(0,+\infty)$. These trajectories are included in the first quadrant of the q plane as shown in Fig. 10(b). There are symmetric counterparts of the trajectories in the other quadrants, and the application of the result here to these is straightforward.

From the condition $H(q,p)=0$, one obtains $p(q)=\pm i\sqrt{2k}e^{-\gamma q^2/2}$. Then the action $S(q,q')$ defined by

$$S(q,q')=\int_q^{q'}[T(p)-V(q)]\frac{dq}{p} \tag{C1}$$

can be written as

$$S(q,q')=\pm i\sqrt{2k}\int_q^{q'}e^{-\gamma q^2/2}dq. \tag{C2}$$

Let l be one of the integrable trajectories projected on the q plane and $q_x=(x,x)$ be the intersection point between l and the axis $\mathrm{Re}\,q=\mathrm{Im}\,q$. Denoting $q_0=(0,0)$ and $q_\infty=(+\infty,0)$, and deforming an integral path, $S(q_0,q_\infty)$ is represented as

$$S(q_0,q_\infty)=S(q_0,q_x)+S(q_x,q_\infty), \tag{C3}$$

where $S(q_0,q_x)$ and $S(q_x,q_\infty)$ are integrated along the axis $\mathrm{Re}\,q=\mathrm{Im}\,q$ and the path l, respectively. One immediately obtains that

$$S(q_0,q_\infty)=\pm i\alpha, \tag{C4a}$$

$$S(q_0,q_x)=\pm\alpha\{[-C(y)+S(y)]+i[C(y)+S(y)]\}, \tag{C4b}$$

where $\alpha=\sqrt{\pi k/\gamma}$, $y=\sqrt{2\gamma/\pi}x$, and $C(y)$, and $S(y)$ are defined by $\int_0^y\cos(\pi t^2/2)dt$ and $\int_0^y\sin(\pi t^2/2)dt$, respectively (Fresnel's functions). From Eqs. (C3) and (C4), one obtains

$$\mathrm{Im}\,S(q_x,q_\infty)=\pm\alpha[1-C(y)-S(y)]. \tag{C5}$$

For our parameter values $k=500$ and $\gamma=0.005$, the trajectory l satisfies $y>1.0$. Since $0.6<[C(y)+S(y)]<1.4$ in this range of y, one obtains that

$$2|\mathrm{Im}\,S(q_x,q_\infty)|<450. \tag{C6}$$

In particular, $\mathrm{Im}\,S(q_x,q_\infty)$ vanishes as $x\to+\infty$, since $C(y)$ and $S(y)$ converge to 1/2 in this limit.

[1] M.C. Gutzwiller, *Chaos in Classical and Quantum Mechanics* (Springer-Verlag, New York, 1990).
[2] M. Wilkinson, Physica A **21D**, 341 (1986); **27**, 201 (1987).
[3] W.A. Lin and L.E. Ballentine, Phys. Rev. Lett. **65**, 2927 (1990).
[4] O. Bohigas, S. Tomsovic, and D. Ullmo, Phys. Rep. **223**, 43 (1993); S. Tomsovic and D. Ullmo, Phys. Rev. E **50**, 145 (1994).
[5] A. Shudo and K.S. Ikeda, Phys. Rev. Lett. **74**, 682 (1995); Physica D **115**, 234 (1998); Prog. Theor. Phys. Suppl. **139**, 246 (2000).
[6] E. Doron and S.D. Frischat, Phys. Rev. Lett. **75**, 3661 (1995); S.D. Frischat and E. Doron, Phys. Rev. E **57**, 1421 (1998).
[7] S.C. Creagh and N.D. Whelan, Phys. Rev. Lett. **77**, 4975 (1996); **82**, 5237 (1999).
[8] S.C. Creagh, in *Tunneling in Complex Systems*, edited by S. Tomsovic (World Scientific, Singapore, 1998) p. 35.
[9] C. Dembowski *et al.*, Phys. Rev. Lett. **84**, 867 (2000).
[10] A. Mouchet *et al.*, Phys. Rev. E **64**, 016221 (2001); **67**, 046216 (2003).
[11] W.K. Hensinger *et al.*, Nature (London) **412**, 52 (2001).
[12] D.A. Steck, W.H. Oskay, and M.G. Raizen, Science **293**, 274 (2001); Phys. Rev. Lett. **88**, 120406 (2002).
[13] K. Takahashi and K.S. Ikeda, Found. Phys. **31**, 177 (2001); K. Takahashi, A. Yoshimoto, and K.S. Ikeda, Phys. Lett. A **297**, 370 (2002); K. Takahashi and K.S. Ikeda, J. Phys. A **36**, 7953 (2003).
[14] O. Brodier, P. Schlagheck, and D. Ullmo, Phys. Rev. Lett. **87**, 064101 (2001); Ann. Phys. (N.Y.) **300**, 88 (2002).
[15] W.H. Miller and T.F. Gorge, J. Chem. Phys. **56**, 5668 (1972); W.H. Miller, Adv. Chem. Phys. **25**, 69 (1974).
[16] T. Onishi, A. Shudo, K.S. Ikeda, and K. Takahashi, Phys. Rev. E **64**, 025201(R) (2001).
[17] S. Adachi, Ann. Phys. (N.Y.) **195**, 45 (1989).
[18] A. Shudo, Y. Ishii, and K.S. Ikeda, J. Phys. A **35**, L225 (2002); (unpublished).
[19] J. Milnor, *Dynamics in One Complex Variable* (Friedr. Vieweg & Sohn, Braunschweig, 1999).
[20] See, for example, A.J. Lichtenberg and M.A. Liberman, *Regular and Chaotic Dynamics* 2nd ed. (Springer-Verlag, New York, 1992), Chap. 3.
[21] See, for example, M. Tabor, *Chaos and Integrability in Nonlinear Dynamics* (Wiley InterScience, New York, 1989), Chap. 6.
[22] A. Katok and B. Hasselblatt, *Introduction to the Modern Theory of Dynamical Systems* (Cambridge University Press, Cambridge, 1999).
[23] V.G. Gelfreich, V.F. Lazutkin, C. Simó, and M.B. Tabanov, Int. J. Bifurcation Chaos Appl. Sci. Eng. **2**, 353 (1992); V.F. Lazutkin and C. Simó, *ibid.* **7**, 253 (1997).
[24] J. Heading, *An Introduction to Phase-Integral Methods* (Metheun, London, 1962).
[25] A. Shudo and K.S. Ikeda, Phys. Rev. Lett. **76**, 4151 (1996); (unpublished).
[26] P. Cvitanovic, G.H. Gunaratne, and I. Procaccia, Phys. Rev. A **38**, 1503 (1988).
[27] F. Christiansen and A. Politi, Nonlinearity **9**, 1623 (1996); Physica D **109**, 32 (1997).
[28] A. Shudo, T. Onishi, K.S. Ikeda, and K. Takahashi, in *Fundamental Aspects of Quantum Physics*, edited by L. Accardi and S. Tasaki (World Scientific, Singapore, 2003), p. 157.
[29] R.L. Devaney and M. Krych, Ergod. Theory Dyn. Syst. **4**, 35 (1984).